UNIVERSITÀ DEGLI STUDI DI PADOVA

Dipartimento di Fisica e Astronomia "Galileo Galilei"

Master Degree in Astrophysics and Cosmology

Final dissertation

Feasibility study of observing binary systems with the ASTRI Mini-array

Thesis supervisor

Prof. Giampiero Naletto

Thesis co-supervisor

Dr. Michele Fiori

Candidate

Matteo Faccioni

Academic Year 2022/23

Ringraziamenti

Come in ogni scalata che si rispetti, il magnifico paesaggio della vetta non può essere raggiunto senza dei favolosi compagni di cordata.

Grazie a Popo & Mari, Kevin, Laura, Tepo, Terri, Sandra, e Edo. Compagni di viaggio in quest'anno e nel futuro, avete reso anche il percorso pieno di sorprese, lasciandomi pieno di speranza.

Un grande grazie al Prof. Naletto, per avermi guidato in tutti questi anni accademici, dimostrandosi una guida attenta e piena di buoni consigli.

Grazie a Michele Fiori, anche se la puntigliosità e la cura non sono più tanto valorizzate al giorno d'oggi, gran parte di questa tesi è merito tuo.

Grazie alla mia famiglia, Emanuele, Anna, Papà e Mamma, per avermi trasmesso i valori che illuminano il cammino.

Per finire, un grazie fraterno a Francesco, un pò un mentore, una spalla nei momenti del bisogno e sicuramente un grande amico.

Contents

Introduction **i**

1 Intensity Interferometry: a quantum effect **1**
- 1.1 Wave interpretation 1
- 1.2 Particle interpretation 3

2 Astronomical applications of intensity interferometry techniques **7**
- 2.1 Hanbury-Brown and Twiss first experiments 7
- 2.2 II at Asiago: Aqueye+ and Iqueye 9
- 2.3 ASTRI Mini-Array 10
  - 2.3.1 The ASTRI Stellar Intensity Interferometer (SI3) configuration . 11
  - 2.3.2 The instrument design 12
  - 2.3.3 The scientific targets 14

3 The ASTRI SI3 simulator **15**
- 3.1 The software architecture 15
  - 3.1.1 The environmental block 15
  - 3.1.2 The correlation function block 21
  - 3.1.3 The fit block 29

4 Results **33**
- 4.1 Uniform disk simulation 33
  - 4.1.1 Variable diameters 33
  - 4.1.2 Variable star fluxes 35
- 4.2 Binary system preliminary simulations 35
  - 4.2.1 Variable diameters 36
  - 4.2.2 Variable flux ratio 36
  - 4.2.3 Variable position angle 36
  - 4.2.4 Variable angular separation 38
- 4.3 Selected binary systems 38
  - 4.3.1 HD 37742 39
  - 4.3.2 HD 144217 39
  - 4.3.3 HD 24912 39
  - 4.3.4 Binary systems preliminary analysis 41
- 4.4 HD 144217 characterization 43
- 4.5 HD 37742 characterization 47

5 Conclusions **49**

A II analogical implementation **51**

B Momentum analysis **53**

C The *emcee* package **55**

Bibliography **57**

Introduction

Theorized by Glauber in the 1960s, Intensity Interferometry (II) has found applications in a wide variety of fields. The first to use it for astronomical measurements, albeit in its “analog” form, were Hanbury-Brown and Twiss [1], culminating their research by measuring the angular diameter of more than thirty stars from the Narrabri observatory, in Australia. Very recently, a research group at the University of Padua and at the Observatory of Padova of the National Institute of Astrophysics obtained the first astronomical II measurements by means of a “quantum” approach, measuring the second order correlation function of Vega using two ultrafast photon counting photometers coupled to two mid-class telescopes available at Asiago (Italy). Nowadays, due to the planned construction of large telescope arrays, and thanks to the enormous advances in electronics, II is acquiring a central role, with great prospects for the further characterization of various celestial bodies. In this context, the objective of this thesis is to evaluate, through simulations, the capabilities of the ASTRI Mini-array telescope system to characterize binary systems using the II technique.

The thesis is structured as follows. In the first chapter, the physical concept behind II is explained, and in the second chapter, some applications of this technique are illustrated. In the third chapter, the structure of the software for simulating II data for the ASTRI Mini-array is presented, and in the fourth chapter, the results of some simulations of binary systems are commented on. Finally, in the conclusion chapter, what has been achieved with this work and the future prospects for the ASTRI Mini-array are discussed.

Chapter 1

Intensity Interferometry: a quantum effect

The behavior of light fluctuations has been extensively described by Mandel's monography [2]. The following is just a brief resume of his work.

Radiation fluctuations were first investigated by Einstein, who first applied the energy fluctuation formula to the black body radiation of an enclosure in thermal equilibrium. The investigation mainly concerned the limitations that these fluctuations impose on the accuracy of radiation measurements. However, after the first successful experiments of Hanbury-Brown and Twiss in the field of intensity interferometry, it rapidly became of great interest. Hanbury-Brown and Twiss followed a classical approach, considering the phenomenon using wave theory. Even if the classical, wave, picture can account quantitatively for many of the observed effects, it fails in accounting for the statistical errors in the fluctuations measurement and for those effects which are concerned with discrete quantum events. The first who treated light fluctuations considering the particle behavior (i.e. quantum) was Purcell [3].

This chapter is divided as follows: in the first section the classical interpretation is described, while in the second one, the particle interpretation is presented.

1.1 Wave interpretation

Assuming the light being emitted from a thermal source, the beam can be considered as a superposition of waves of many different frequencies ν, lying within some continuous range $\Delta\nu$. Not having a definite phase relationship between the frequency components, the resultant wave amplitude $V^{(r)}(t)$, where the apex (r) indicates the wave real component, in the interval T, can be described by a Fourier series as:

$$V^{(r)}(t) = \sum_n a_n cos(2\pi nt/T) + b_n sin(2\pi nt/T)\,. \tag{1.1}$$

For a stationary process, and a sufficiently long T, the Fourier coefficients a_n and b_n can be considered statistically independent Gaussian random variables with the same variance. Then, assuming the light to be linearly polarized, consider two points P_1 and P_2, and the respective light waves function $V_1(t)$ and $V_2(t)$ at these points. The mutual coherence function of the two waves is defined as:

$$\Gamma_{12}(\tau) = \langle V_1(t+\tau)V_2^*(t)\rangle\,, \tag{1.2}$$

and the normalized coherence function is:

$$\gamma_{12}(\tau) = \Gamma_{12}(\tau)/\sqrt{\langle I_1\rangle\langle I_2\rangle}\,, \tag{1.3}$$

where $\langle I_1\rangle$ and $\langle I_2\rangle$ are the time averaged intensities at P_1 and P_2. These can be computed as:

$$\langle I_i(t)\rangle = \lim_{T\to\infty}\frac{1}{T}\int_{-\frac{T}{2}}^{\frac{T}{2}} I_i(t)dt\,. \tag{1.4}$$

The instantaneous intensities can be written respectively as:

$$I_1(t) = V_1(t)V_1^*(t)\,, \tag{1.5}$$

$$I_2(t) = V_2(t)V_2^*(t)\,, \tag{1.6}$$

hence the mutual coherence function of the intensities, i.e. the second order coherence function of the waves amplitude, is:

$$\begin{aligned} \langle I_1(t+\tau)I_2(t)\rangle &= \left\langle V_1(t+\tau)V_1^*(t+\tau)V_2(t)V_2^*(t)\right\rangle = \\ &= \left\langle V_1^{(r)^2}(t+\tau)V_2^{(r)^2}(t)\right\rangle + \left\langle V_1^{(r)^2}(t+\tau)V_2^{(i)^2}(t)\right\rangle + \\ &+ \left\langle V_1^{(i)^2}(t+\tau)V_2^{(r)^2}(t)\right\rangle + \left\langle V_1^{(i)^2}(t+\tau)V_2^{(i)^2}(t)\right\rangle . \end{aligned} \tag{1.7}$$

where the (r) and (i) apexes indicate the wave real and imagery parts respectively. It can be shown that the correlation functions are related to the mutual coherence function by:

$$\left\langle V_1^{(r)^2}(t+\tau)V_2^{(r)^2}(t)\right\rangle = \left\langle V_1^{(i)^2}(t+\tau)V_2^{(i)^2}(t)\right\rangle = \frac{1}{2}\,\mathrm{Re}[\Gamma_{12}(\tau)]\,, \tag{1.8}$$

$$-\left\langle V_1^{(r)^2}(t+\tau)V_2^{(i)^2}(t)\right\rangle = \left\langle V_1^{(i)^2}(t+\tau)V_2^{(r)^2}(t)\right\rangle = \frac{1}{2}\,\mathrm{Im}[\Gamma_{12}(\tau)]\,. \tag{1.9}$$

Finally, by means of equations (1.8) and (1.9), equation (1.7) can be written as:

$$\langle I_1(t+\tau)I_2(t)\rangle = \langle I_1\rangle\langle I_2\rangle + |\Gamma_{12}(\tau)|^2 = \langle I_1\rangle\langle I_2\rangle\left[1+|\gamma_{12}(\tau)|^2\right] . \tag{1.10}$$

In the same way, it is possible to write the correlation between the fluctuations of I_1 and I_2, expressed as $\Delta I_i = I_i(t) - \langle I_i\rangle$, in the following way:

$$\langle \Delta I_1(t+\tau)\Delta I_2(t)\rangle = \langle I_1(t+\tau)I_2(t)\rangle - \langle I_1\rangle\langle I_2\rangle = \langle I_1\rangle\langle I_2\rangle\,|\gamma_{12}(\tau)|^2 . \tag{1.11}$$

Considering now unpolarized light, the previous equation takes the form:

$$\langle \Delta I_1(t+\tau)\Delta I_2(t)\rangle = \frac{1}{2}\langle I_1\rangle\langle I_2\rangle\,|\gamma_{12}(\tau)|^2 . \tag{1.12}$$

This equation establishes the basic principles on which an intensity interferometer depends. In appendix A it is reported how Hanbury-Brown and Twiss used this equation to measure stellar diameters.

In practical application, equation (1.12) does not fully agree with the experimental results. This is due to two reasons:

- the wave interpretation cannot describe the large fluctuations in the output of a photo-multiplier. These arise primarily from the shot noise of the photo-current and can only be described by assuming the quantum nature of the radiation;

- equation (1.10) describes the correlation of the instantaneous intensities $I(t)$. Although $I(t)$ changes slowly compared with the wave function $V(t)$, yet its fluctuations are normally too rapid for an electronic correlator to follow. Roughly speaking, the frequency spread of the fluctuations of $I(t)$ is of the same order as the frequency spread $\Delta\nu$ of the incident light. The signal on which the electronic correlator operates is therefore already some short time average of $I(t)$.

To solve these issues a particle, or quantum, approach is needed. This is described in the next section.

1.2 Particle interpretation

Since only the results of the interactions between photons with the photo-detector are observed, the following discussion will refer to the interaction products, i.e. the photo-electrons. To compute the probability of detecting a photon by its interaction at a certain point at a certain time, a wave function for the photons of the radiation field must be defined. The photon wave function $\psi(\mathbf{k}, t)$, in the momentum-spin space can be defined as:

$$\psi(\mathbf{k}, t) = \sqrt{\left(\frac{2}{k\hbar}\zeta(\mathbf{k})exp(ickt)\right)}, \tag{1.13}$$

where $\mathbf{k}$ is the wave vector, whose magnitude, k, is the wave number $2\pi\nu/c$, and $\zeta(\mathbf{k})$ represents the Fourier coefficients.

The Fourier transform of equation (1.13) is:

$$\Psi(\mathbf{r}, t) = \frac{1}{(2\pi)^3}\int\int\int_{-\infty}^{\infty} \psi(\mathbf{k}, t)exp(-i\mathbf{k}\cdot\mathbf{r})d\mathbf{k}, \tag{1.14}$$

It can be shown that $\psi(\mathbf{k}, t)$ is a Schrödinger type equation of motion and that $\psi^*(\mathbf{k}, t)\psi(\mathbf{k}, t)d\mathbf{k}$ can be interpreted as the probability of finding the photon in the momentum interval $d\mathbf{k}$. Being interested in determining the position with an accuracy of the order of a wavelength, $\Psi^*(\mathbf{r}, t)\Psi(\mathbf{r}, t)$ can be treated as the spatial probability density.

A real light beam is composed of many photons not in a pure quantum state. Considering non-interacting photons it is possible to write down a symmetrized momentum-spin Schrödinger wave function, consisting of products of the functions $\psi_i(\mathbf{k}, t)$. From this, the probability of finding one photon in the momentum interval $d\mathbf{k}$ is found to be $\sum_i \psi_i^*(\mathbf{k}, t)\psi_i(\mathbf{k}, t)d\mathbf{k}$, where the sum is to be taken over all the photons of the system.

Supposing now the photons are in a mixed quantum state, this implies that the state can be described by a statistical ensemble of Schrödinger wave functions and that all the probabilities must be computed by averaging over the ensemble. Representing each photon wave function as $\psi_i^*(\mathbf{k}, t)$, then the probability of finding one photon in the momentum interval $d\mathbf{k}$ is $N\langle\psi^*(\mathbf{k}, t)\psi(\mathbf{k}, t)\rangle\, d\mathbf{k}$, where the square brackets denote the ensemble average and N is the number of particles. Now, from equation (1.14), the ensemble of functions $\psi(\mathbf{k}, t)$ generates an ensemble of functions $\Psi(\mathbf{r}, t)$. It follows that the probability of finding one photon within the space interval $d\mathbf{r}$ is given by the ensemble average $N\langle\Psi^*(\mathbf{r}, t)\Psi(\mathbf{r}, t)\rangle\, d\mathbf{r}$.

If all the Fourier coefficients $\zeta(\mathbf{k})$ of $\Psi(\mathbf{r}, t)$ are statistically independent for different k, then the central limit theorem of statistics states that its expansion would generate a Gaussian random function. Since photons of different energies produced by thermal sources are normally independent, it follows that $\Psi(\mathbf{r}, t)$ is to be regarded as a Gaussian random function for thermal light.

For a plane, linearly polarized, quasi monochromatic beam of thermal light, it can be shown that the classical wave function representation, $V(\mathbf{r}, t)$, and $\Psi(\mathbf{r}, t)$ are equivalent apart from a constant and have identical statistical properties. Hence, being their statistical properties similar, the probability of detecting a photon at $\mathbf{r}$ at time t, which is proportional to $\Psi^*(\mathbf{r}, t)\Psi(\mathbf{r}, t)$, is also proportional to $V^*(\mathbf{r}, t)V(\mathbf{r}, t) = I(\mathbf{r}, t)$. Photons can only be detected by their interactions with charges, but, if the higher order interactions are ignored, the probability that a photon of given momentum falling on a photo-cathode ejects a photo-electron will be just a constant α, representing the quantum sensitivity of the cathode. If the intensity $I(t)$ of the quasi-monochromatic light beam is measured in units of photons per second, then the probability that this beam, falling on the photo-electric detector, gives rise to a count in an interval dt, is simply $\alpha I(t)dt$.

Hence, the quantity $I(t)$ bridges the gap between the particle and the wave models and

many of the previous results based on the wave picture now become applicable. The two models can be seen to have much in common, but the output of a photo-detector is no longer to be regarded as a continuous function of time and the discrete quantum phenomena, such as shot noise, can now be examined.
The statistics of the counts obtained with a photodetector illuminated by a light beam are described by the probability distribution $p(n,T)$ of obtaining n counts in a time interval T. We can define now a time dependent probability distribution $p(n,T,t)$, which denotes the probability that n counts are detected in the time interval $[t, t+T]$. It then follows that $p(1, dt, t) = \alpha I(t)$.
It can be shown that the probability distribution $p(n,T,t)$ is a Poisson distribution, with parameters given by the expectation value of n in the interval t to $t+T$. This is equal to:

$$n = \alpha \int_t^{t+T} I\,(t')\,dt'\,, \tag{1.15}$$

thus:

$$p(n,T,t) = \frac{1}{n!}\left[\alpha \int_t^{t+T} I\,(t')\,dt'\right]^n exp\left[-\alpha \int_t^{t+T} I\,(t')\,dt'\right]. \tag{1.16}$$

Being $I(t)$ a random function, the probability $p(n,T,t)$ is itself a random function, and $p(n,T)$ must be obtained by it by taking its time average.
However, the probability $p(n,T)$ for a general T is not easily computed. But being interested in the count variance, this can be treated with the generating momentum, as described in the appendix B. Following this approach, the variance $\left\langle (\Delta n)^2 \right\rangle$ results equal to:

$$\left\langle (\Delta n)^2 \right\rangle = \alpha\langle I\rangle T + \alpha^2 \langle I\rangle^2 \int\int_{-\frac{1}{2}T}^{\frac{1}{2}T} |\gamma_{11}(t_1 - t_2)|^2 dt_1 dt_2 = \langle n\rangle[1 + \langle n\rangle \xi(T)/T]\,, \tag{1.17}$$

where, according to [4], $\xi(T)$ is equal to:

$$\xi(T) = \frac{2}{T}\int_0^T (T - t')\left|\gamma_{11}\,(t')\right|^2 dt'\,. \tag{1.18}$$

Finally, the count variance can be expressed as:

$$\left\langle (\Delta n)^2 \right\rangle = \begin{cases} \langle n\rangle(1 + \langle n\rangle) & T \ll 1/\Delta\nu \\ \langle n\rangle[1 + \langle n\rangle \xi(\infty)/T] & T \gg 1/\Delta\nu \end{cases}. \tag{1.19}$$

where the first equation can be recognized as characteristic of the Bose-Einstein distribution, while the second is the characteristic expression for n bosons distributed among $T/\xi(\infty)$ cells of phase space, so that $\xi(\infty)$ should be identified as the coherence time of light.
The time dependent probability distribution expressed in equation (1.16) allows us to calculate the correlation of the number of counts n_1 and n_2, recorded by two photodetectors illuminated by partially coherent light beams for a time T. The expectation value of the product $\langle n_1 n_2\rangle$ is:

$$\langle n_1 n_2\rangle = \sum_{n_1=0}^{\infty}\sum_{n_2=0}^{\infty} n_1 n_2 \left\langle p_1(n_1,T,t) p_2(n_2,T,t)\right\rangle\,. \tag{1.20}$$

By inserting the mean values of the Poisson distribution, it is possible to write:

$$\langle n_1 n_2\rangle = \alpha_1\alpha_2 \int\int_t^{t+T} \langle I_1(t') I_2(t'')\rangle\, dt' dt'' = \alpha_1\alpha_2 \int\int_t^{t+T} \langle I_1(t + t' - t'') I_2(t)\rangle\, dt' dt''\,. \tag{1.21}$$

Assuming now that the spectral distributions of the two beams are equal, the normalized coherence function can be written as:

$$\gamma_{12}(\tau) = \gamma_{12}(0)\gamma_{11}(\tau)\,. \tag{1.22}$$

By substituting it in equation (1.21), it results:

$$\begin{aligned}\langle n_1 n_2\rangle &= \alpha_1\alpha_2\langle I_1\rangle\langle I_2\rangle\Delta T^2 + \alpha_1\alpha_2\langle I_1\rangle\langle I_2\rangle|\gamma_{12}(0)|^2 \int\int_0^{\Delta T} \left|\gamma_{11}\left(t' - t''\right)\right|^2 dt'dt'' \\ &= \langle n_1\rangle\langle n_2\rangle + \langle n_1\rangle\langle n_2\rangle[\xi(\Delta T)/\Delta T]|\gamma_{12}(0)|^2\,,\end{aligned} \tag{1.23}$$

then, the correlation of the fluctuations $\langle\Delta n_1\Delta n_2\rangle$ is given by:

$$\langle\Delta n_1\Delta n_2\rangle = \langle n_1 n_2\rangle - \langle n_1\rangle\langle n_2\rangle = \langle n_1\rangle\langle n_2\rangle[\xi(\Delta T)/\Delta T]|\gamma_{12}(0)|^2\,. \tag{1.24}$$

This is analogous to the correlation equation used by Hanbury-Brown and Twiss (equation (A.7)), except that it is applied to linearly polarized light.
The first order correlation function $\gamma_{12}(0)$ is related to the source brightness distribution through the Van Cittert Zernike theorem.
This fundamental theorem, named by Van Cittert - Zernike [6], states that for a noncoherent and almost monochromatic extended source, the complex visibility, μ, is the normalized Fourier transform of the brightness distribution of the source, I. The complex visibility is a measure of the contrast of interference in any system subject to wave superposition. It can be defined as:

$$\mu = \frac{I_{max} - I_{min}}{I_{max} + I_{min}}\,, \tag{1.25}$$

where I_{max} is the maximum intensity of the oscillations and I_{min} the minimum intensity of the oscillations.
The Van Citert-Zernike theorem can be then expressed as:

$$\mu(u, v) = \int_{-\infty}^{\infty}\int_{-\infty}^{\infty} I(\alpha,\beta)exp(2\pi i(\alpha u + \beta v))d\alpha d\beta\,, \tag{1.26}$$

where (α,β) represent angular coordinates on the sky, and (u, v) represent spatial frequencies.
By considering the correlation has been computed in the interval ΔT, equation (1.23) can be written as:

$$|\gamma_{12}(0)|^2 = \left[\frac{\langle n_1 n_2\rangle}{\langle n_1\rangle\langle n_2\rangle}\frac{T}{\Delta T} - 1\right]\frac{\Delta T}{\tau_0}\,. \tag{1.27}$$

This equation will be used to compute the second order correlation function, and then to fit the star diameter from it.

Chapter 2

Astronomical applications of intensity interferometry techniques

Intensity interferometry is an ideal tool for achieving angular resolutions that are not possible with traditional imaging techniques. This is also simplified by the fact that it is not necessary to have very high-quality optical surfaces to make II measurements, besides the fact that seeing does not have a big impact, contrary to amplitude interferometry techniques that instead require very high-quality optical paths.
In fact, in an intensity interferometer, the optical quality of the telescope is not really important as any imperfections in the optical path of the incoming light can be acceptable down to a few centimeters since the time resolution given by the acquisition electronics is always in the order of a nanosecond, corresponding to $\sim$ 30 cm traveled by the light.

2.1 Hanbury-Brown and Twiss first experiments

Hanbury-Brown and Twiss were the first to use II technique for astronomical measurements between the 50s and the 70s. As explained in Hanbury-Brown's book [7], the concept was initially born to overcome the need for highly stable oscillators for very long baseline interferometers in the radio domain. During their first experiments, they noticed that the system was also insensitive to atmospheric scintillations. Also, considering that they did not need high optical quality but only a large enough collecting area, they decided to build an interferometer in the optical band, which led to the development of the Narrabri Observatory.
Nevertheless a lot of initial criticism, Hanbury-Brown and Twiss succeeded in designing and building the first optical II at Narrabri, a small country town on the river Namoi in the northern New South, Australia. By using two movable 6.5 meters mirrors as collectors, they were able to obtain baselines between 10 and 188 meters. During a decade of observations [8], they measured the radii of 32 single O-F spectral type stars, making the first ever measurements of a main sequence star. Moreover, the experiment demonstrated the potentialities of what a larger intensity interferometer could do, such as limb darkening, stellar rotation, and polarization characterization, or the observation of pulsations in radius of a Cepheid variable [7].
The Narrabri observatory consisted of:

- two reflectors, composed of regular 12-sided polygons, with a diameter of 6.5 m;
- two interference filters, with a central wavelength of 443 nm, and a 5 nm bandwidth;
- two photomultipliers, on which the collected light was focused;
- a correlator, which correlated in real time the two current signals from the photomultipliers;
- a data handling system, which displayed the measured data.

The Narrabri II was operated in the *analog* mode, whereby the currents of the two photomultipliers were directly correlated. Its configuration is shown in Figure (2.1).

The instrument worked as follows: the light from the star is received on two separated collectors and it is focused at each onto a photomultiplier. Then the two signals are

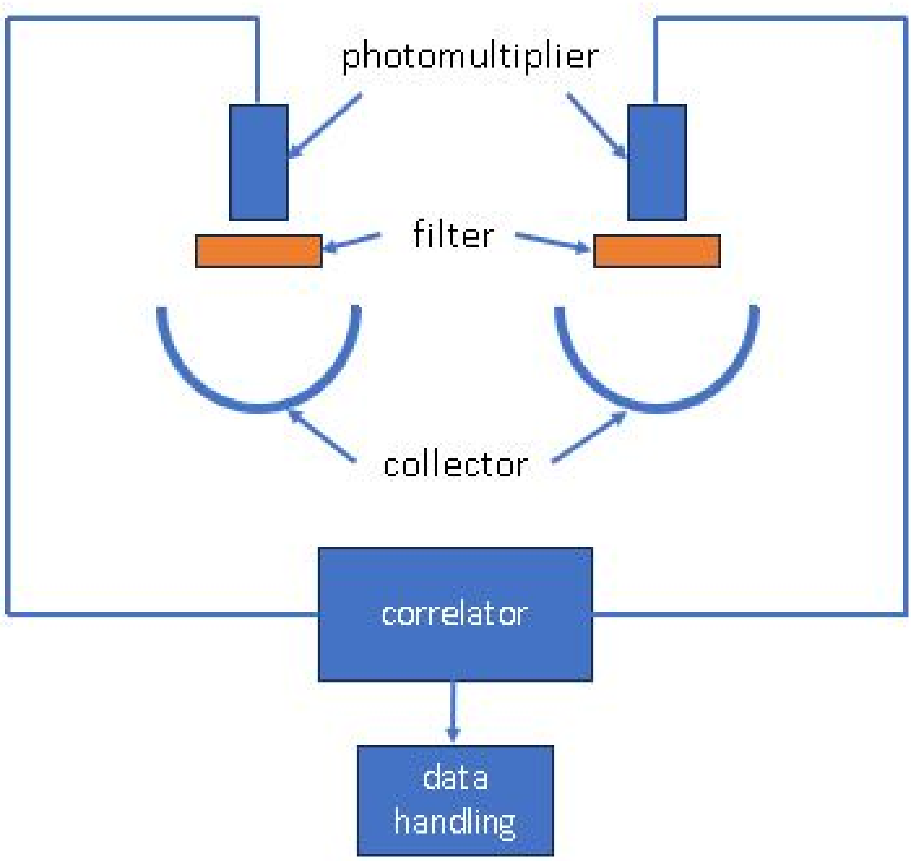
photomultiplier
filter
collector
correlator
data handling

Fig. 2.1. *Narrabri II concept: the system acquires the light by means of two collectors, and the two signals generated by the photomultipliers are input to a correlator.*

connected to the inputs of a correlator. The correlation was recorded by an integrating motor, while the RMS value of the noise at the output was recorded by a second integrating motor. The obtained correlation observing Sirius is represented in Figure (2.2).

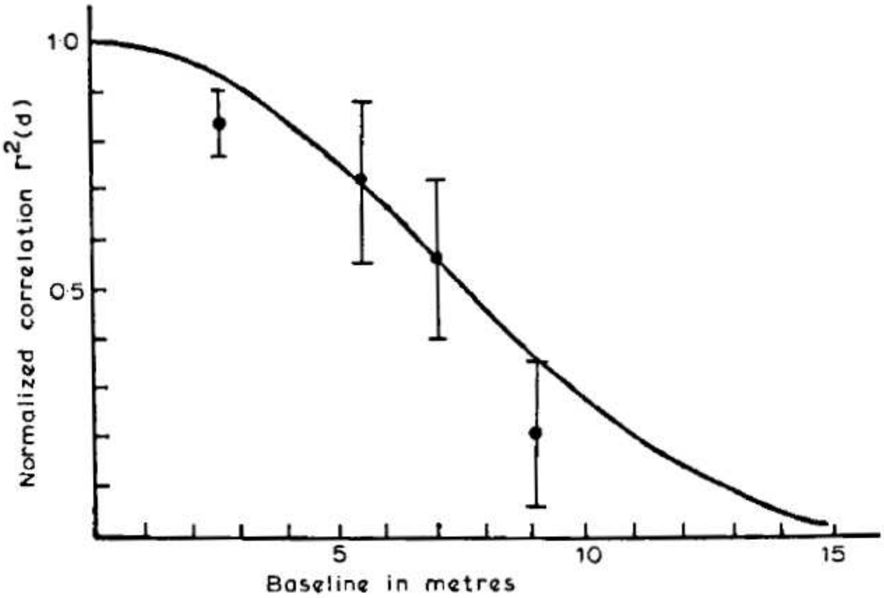

Fig. 2.2. *Narrabri measured correlation: the dots represent the measured correlation at different baselines, while the continuous line represents the ideal correlation [7].*

2.2 II at Asiago: Aqueye+ and Iqueye

Since 2005, a team of researchers from the University of Padova and from the Italian National Institute of Astrophysics (INAF) in Padova Observatory has been investigating very high time resolution astrophysical phenomena in the optical band [9]. In this context, two instruments were built in order to perform photon counting with sub-nanosecond temporal accuracy [10]. The first, called Aqueye+, is regularly mounted at the 1.8 m Copernicus telescope in Asiago, while the second, Iqueye, was mounted at the ESO New Technology Telescope in Chile, at the William Herschel Telescope, and at the Telescopio Nazionale Galileo on the Roque, Canary Islands. Finally, after delivering extraordinarily accurate results in optical pulsar timing, Iqueye was moved to Asiago and mounted at the 1.2 m Galileo telescope, enabling experiments of optical intensity interferometry on a baseline of a few kilometers, together with the Copernicus telescope.

Aqueye+ and Iqueye are narrow Field Of View (FOV) photon counting photometers with sub-ns absolute time accuracy. They are both composed of a pyramidal mirror, that splits the incoming beam after the telescope focus into four sub-apertures focused on four independent SPADs detectors. This 4-split pupil optical configuration allows to perform a cross-correlation of the signal also at zero baseline (that is among different portions of the same telescope), which is crucial to calibrate the degree of coherence. Then, an acquisition system capable of sub-ns time tagging accuracy with respect to UTC, saves the data.

The Galileo telescope and the Copernicus telescope are located respectively in the resorts of Pennar and Cima Ekar, almost 4 km apart. Equipped with Aqueye+ and Iqueye, the two telescopes provided a suitable site to realize a photon counting km-baseline intensity interferometer. In this context, Aqueye+ has been directly mounted at the Copernicus telescope, while Iqueye has been fiber-coupled with the Galileo telescope by means of the Iqueye Fiber Interface instrument [11].

The latter configuration was used to investigate Vega. The choice of such a bright star is motivated by the need to measure the correlation in a reasonable time using telescopes with a small collecting area. The measurements were performed using two different sets of filters: an $H\alpha$ filter plus a $x10$ neutral density filter (ND1) with a narrow band interferometric filter to calibrate the response of the system and to measure the actual correlation.

The experiment [12] successfully detected the temporal correlation of Vega at zero baseline and performed a measurement of the correlation on a projected baseline of $\sim$ 2km. The computed average discrete degree of coherence at zero baseline for Vega is $\langle g^2 \rangle = 1.0034 \pm 0.0008$, providing a detection with a signal-to-noise ratio (SNR) of 4. The measurements and the SNR are consistent with the expected degree of spatial coherence for a source with the 3.3 mas angular diameter of Vega. Moreover, as shown in Figure (2.3), no correlation is detected over the km baseline.

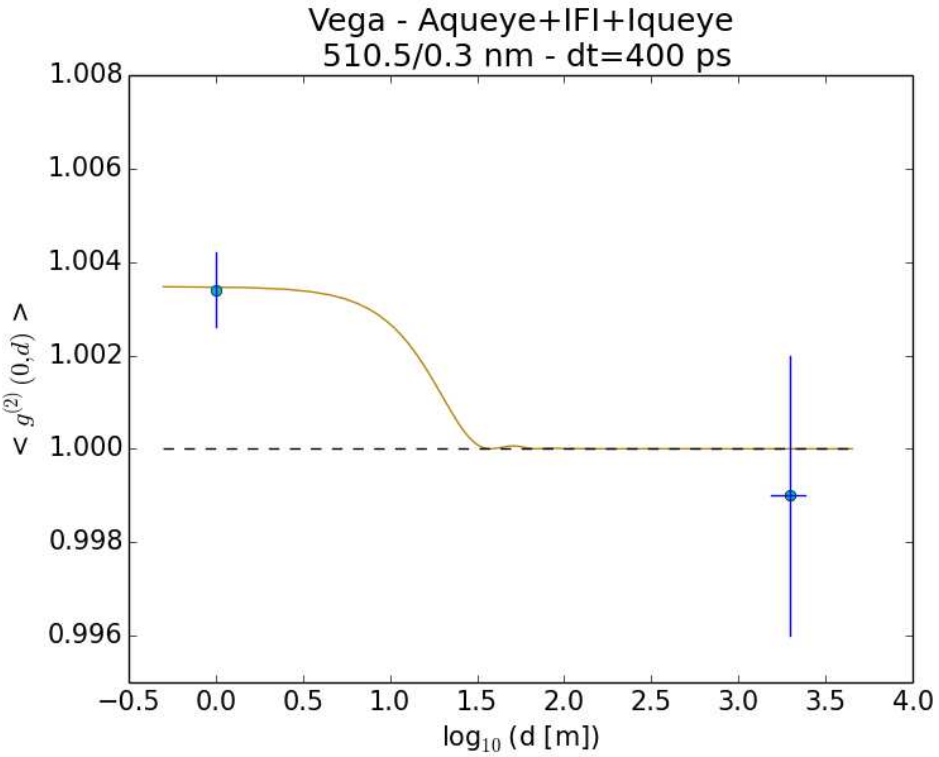

Fig. 2.3. *Asiago II results: the two blue dots with their relative errors represent the measured second order correlation function at the two different baselines [12].*

2.3 ASTRI Mini-Array

This section is just a brief description of the ASTRI Mini-Array system, for more details, refer to [13].

The ASTRI Mini-Array is an international collaboration aimed at the deployment of nine imaging atmospheric Cherenkov telescopes. The name ASTRI, meaning *"Astrofisica con Specchi a Tecnologia replicante Italiana"*, comes from the technology with which the mirrors are manufactured.

Even if devoted primarily to study γ-ray sources at very high energies, it will also give the opportunity to perform measurements using the II technique. The nine telescope configurations will give the opportunity to use 36 different baselines, between 100 and 700 meters, providing an angular resolution below 100 μas. This resolution will enable the possibility to reveal details on the surface and on the environment surrounding bright stars visible in the night sky [1].

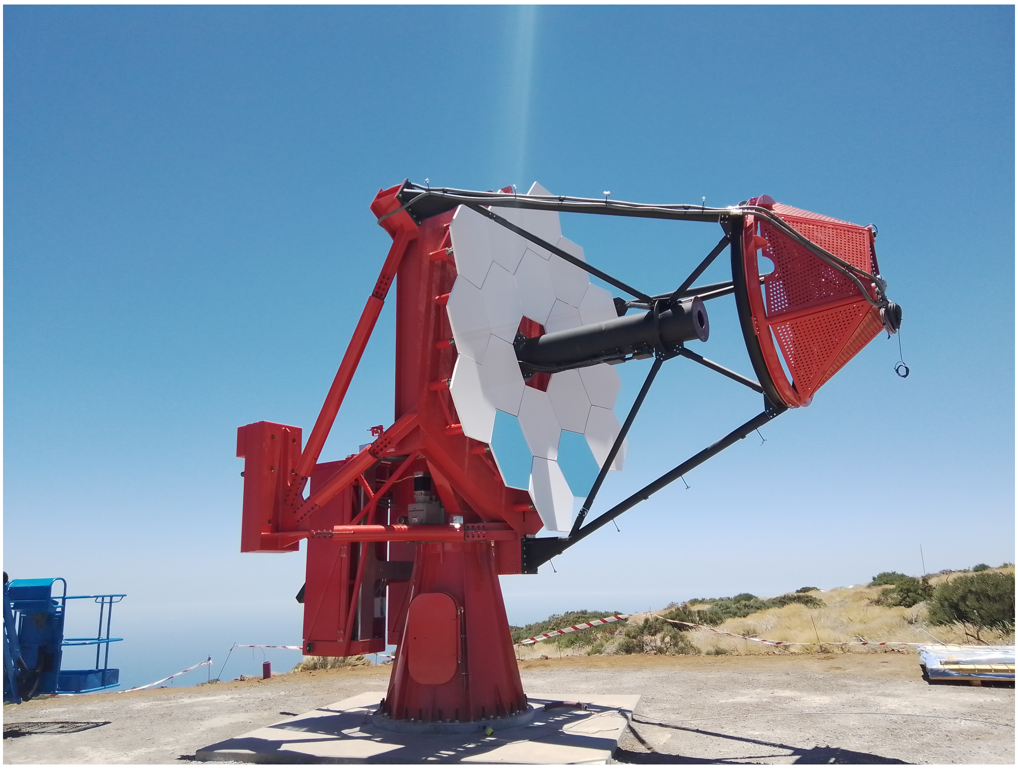

Fig. 2.4. *The first ASTRI telescope mounted at the Teide Observatory.*

2.3.1 The ASTRI Stellar Intensity Interferometer (SI3) configuration

In contrast to the Narrabri interferometer, which worked in *analog* mode, the ASTRI Mini-array SI3 will measure the second order correlation function by a post-process analysis of the arrival times of photons, which will be stored in a suitable archiving system. This approach has the advantage that the data reduction chain could be repeated several times, enabling the possibility of checking for systematics, tuning the parameters of the analysis, optimizing the procedure, and increasing the accuracy of the results. Moreover, working in photon counting, so at the limit of detection, allows observing higher magnitude stars.
The instrument setup consists of:

- nine 4 meter diameter dual-mirrors telescopes;
- an interference filter for each telescope. The spectral band will be very narrow, between 3 and 8 nm, centered at a desired wavelength in the B band;
- four square silicon photomultiplier (SiPM) sensors, in a 4-quadrant configuration. SiPMs are single photon sensitive devices based on single photon avalanche diodes (SPADs). Each SiPM is 3mm wide;
- a complex electronic train that time tags each incoming photon;
- a server to save and post-process the data.

---

[1] As Pedro Casaldaliga said "*o mundo é pequeno quando os motivos de encontro são grandes*". Indeed, almost one year and a half ago, during my work at EIE, I had the privilege to work on the installation and tuning of the first ASTRI Mini-Array telescope. In Figure (2.4) its sunrise, kissed by the Canary Sun, is represented.

2.3.2 The instrument design

The main criteria in the SI3 design were to have an independent and compact instrument, minimizing its size, weight, and interfaces, in order to not affect gamma-ray observations.
The instrument is composed of three different modules:

- the *focal plane module (FPM)*, containing the optics, the detectors, and the read-out electronics.
- the *front end electronics (FEE) module*, which performs the signal conditioning and detects the photons;
- the *back end electronics (BEE) module*, which adds the time tags to the detected photons.

The FPM is positioned on the telescope focal plane, in front of the Cherenkov camera. It will be deployed through a dedicated mechanical arm during the SI3 observations. The optical design is based on a prefocal system, as shown in Figure (2.5).

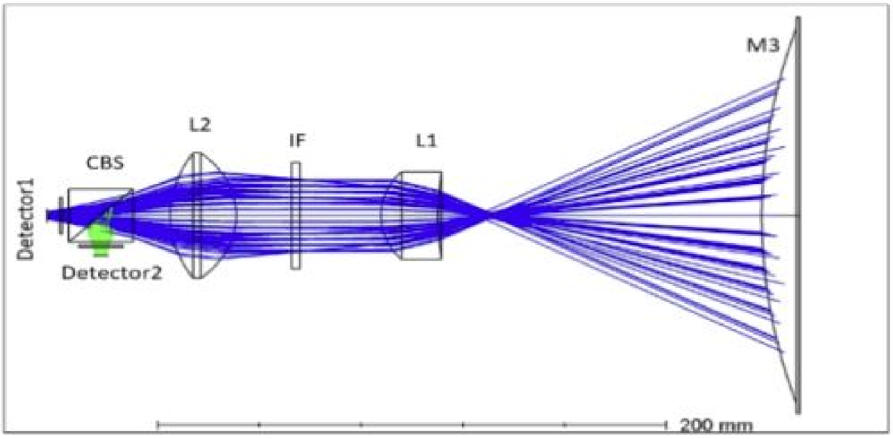

Fig. 2.5. *SI3 focal plane module optical design in the special case of measuring the zero baseline correlation using one telescope [13]*

The instrument is a catadioptric system composed of a spherical convex mirror (M3, 180 mm in diameter), two spherical lenses (L1, L2, 40 – 60 mm in diameter respectively), and one interferometric filter (IF, 40 mm in diameter). As represented in the above figure, the beam from the telescope secondary mirror is intercepted by M3 at the ASTRI camera level before reaching the focus; is then collimated by L1, passes through the interference filter, and finally is refocused by L2 onto the II focal plane, where a four-quadrant SiPM is placed. The detectors have a spectral response range from 270 nm to 900 nm, with peak sensitivity at 450 nm, and are cooled with a single Peltier cell to maintain their temperature at a few degrees Celsius, reducing the dark noise. The signal from the detectors is read by a commercial evaluation board and amplified with four broadband amplifiers.
Having four sensors, it is in principle possible to measure the zero cross correlation for each individual telescope; but as it is not possible to accurately predict the crosstalk noise among the sensors, one telescope of the ASTRI Mini-Array will host a slightly modified camera. The latter contains, in addition to the catadioptric system, a cubic beam splitter to split the light beam into two channels, providing the zero baseline measurement. In addition, the four detectors will allow an alignment control of the instrumentation during measurements, considering that a well centered target will have

similar count rates in all the detectors.
The FEE module is located on the telescope mast. In this module, the signal is input to two high speed comparators (with ~ 300 ps response time) which generate Positive Emitter Coupled Logic (PECL) digital pulses. These pulses are then sent to the BEE module. For a more detailed description of the FEE module and its components refer to [14].
In the BEE module, the electronics tag the detected photons with the required timing accuracy (<< 1 ns) at a rate up to 100 Mct/s. The data stream is then transferred to the Array Data Acquisition System (ADAS) for on-site acquisition and storage. The core of the BEE is a fast Time-to-Digital-Converter board, mounted on an Industrial PC and disciplined with a Pulse-Per-Second and a 10 MHz reference signal from a Time Distribution Unit (TDU). The reference and PPS signals are used to reconstruct the absolute time in the post-processing algorithm. The system will acquire ~ 100 TB of raw data each month that will be transferred and analyzed off-site before the start of the following observing run. Assuming an average data transfer rate of ~ 125 MB/s, all the data are transferred in ~ 10 days.
The raw data acquired by the BEE will be processed to produce reconstructed and calibrated event lists using the time reference signals from the TDU. The obtained final photon time tags will all be referred to UTC and will have an accuracy below 1 ns. After removing low quality data by filtering them through suitable quality checks, the event lists are ready for scientific analysis. They are then segmented into chunks of size adequate for being efficiently handled in the following steps. Then, coincidences are searched for in the arrival times at different telescopes varying the time delay between them. The entire procedure has already been developed and tested in the Asiago intensity interferometry experiment [12], the only caveat will be to scale up the needed hardware, given the large amount of data. What is expected from observing a bright star like Spica for around 18 hours is represented in Figure (2.6).

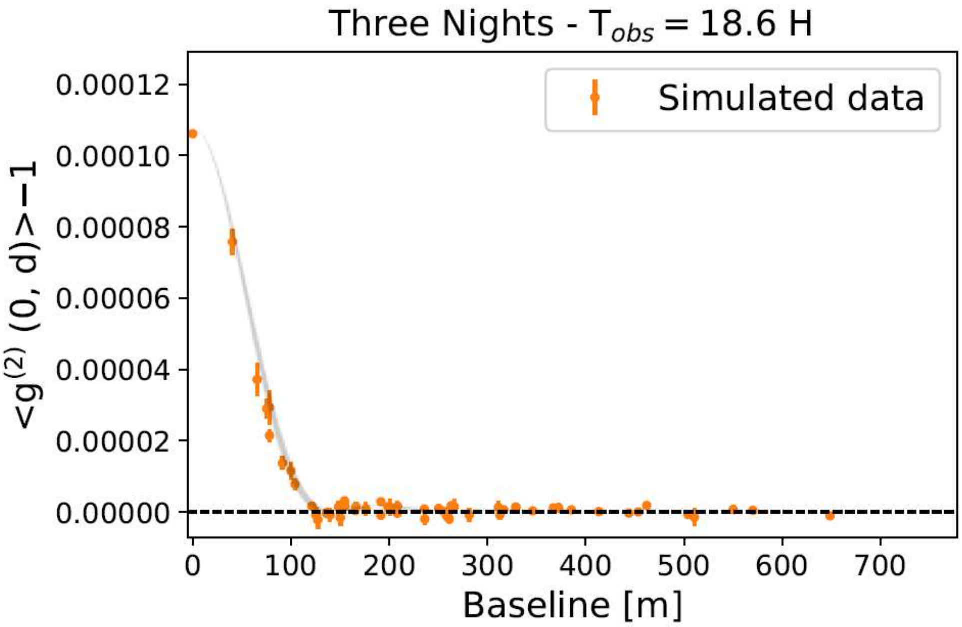

Fig. 2.6. *Spica observed with SI3 simulation. The orange points represent the simulated measured second order correlation function for each of the 36 ASTRI Mini-array baselines.*

The final goal will be to perform image reconstruction of bright stars using ASTRI SI3 data.

2.3.3 The scientific targets

The possibility to measure the angular shape of stars with a resolution of 100 μas on multiple baselines will enable the study of many different aspects of stars, extending in the visible band what today can be done in the near Infrared (IR) band using telescopes such as CHARA, VLTI, and others [15].

Imaging with this resolution allows, for example, the detection of surface features such as dark or bright spots, revealing the possible asymmetry in the surface brightness distribution of the star, and measuring the oblateness of high speed rotating stars. Furthermore, observing the stars' circumstellar discs will reveal details of the disc structure, its density gradients, and scale height, essential data to understand how these systems evolve and dynamically interact. In this context, the ASTRI Mini-array operated in stellar intensity interferometry mode will give an an extraordinary set of data regarding the brightest nearby stars and their environments. Hence, the optimal targets would be stars with high brightness temperature, with a significant photon flux, and structures small enough to produce coherence over long baselines. O-thorough-G type stars of adequate brightness are all suitable and potential targets, which makes the B band, between 420 nm and 500 nm, the appropriate working wavelength window.

Chapter 3

The ASTRI SI3 simulator

To simulate the Astri Mini-array SI3 observational performance a dedicated software has been developed by Dr. Michele Fiori. The software, totally written in python, simulates the entire observation process, from data acquisition to its post-processing. At the moment it is possible to simulate a uniform disk source only, but in the future, it is foreseen the possibility to simulate different source irradiance profiles. The aim of this thesis was to add a module for modeling, simulating, and fitting SI3 data in the case of observations of binary systems, in order to assess the capabilities of ASTRI to study such systems. To this purpose, initially, a 1-dimensional (1D) model has been developed, to assess which binaries were well identifiable given the characteristics of the array. Once the best binary systems have been identified, a 2-dimensional (2D) model was developed to assess their actual observabilities. In the following section, the software architecture is described.

3.1 The software architecture

The software architecture can be subdivided into the following blocks:

- the *environmental block*, where all the environmental variables are computed for each pair of telescopes;
- the *correlation function block*, where the theoretical and simulated correlation functions are computed;
- the *fit block*, where the correlation function is fitted to a model and the target star parameters are obtained.

In Figure (3.1) it is represented the software architecture.

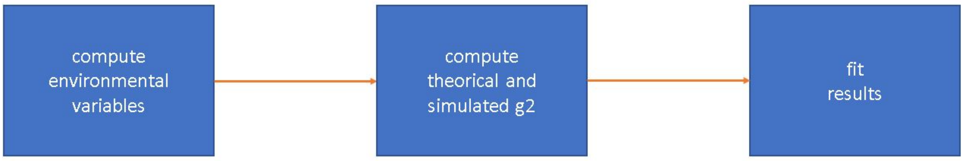
compute environmental variables
compute theorical and simulated g2
fit results

Fig. 3.1. *Model block diagram. Each blue square corresponds to a dedicated function block, that runs specific functions.*

In the following subsections, each block will be explained in more detail.

3.1.1 The environmental block

This block computes all the variables that depend on the environment at the time of the measurement. All the environmental variables are computed with respect to the foreseen ASTRI Mini-array location, as represented in Figure (3.2).

The telescopes are being built at the Izaña observatory, near the Teide volcano, in Tenerife island, ESP. The telescopes coordinates are reported in Table (3.1).

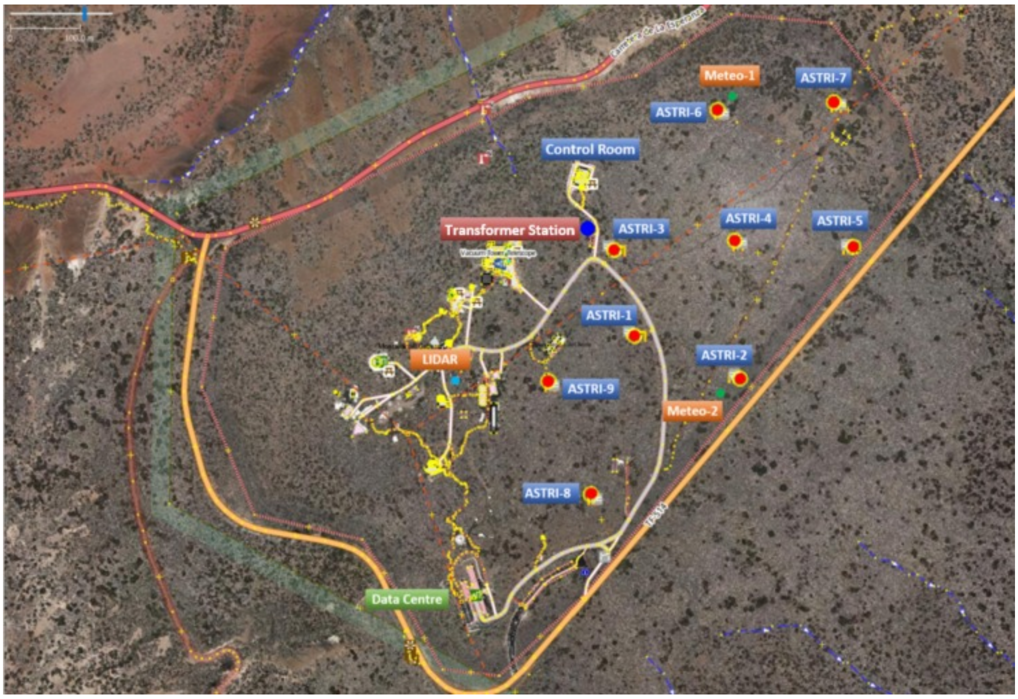
Meteo-1
ASTRI-7
ASTRI-6
Control Room
Transformer Station
ASTRI-3
ASTRI-4
ASTRI-5
ASTRI-1
LIDAR
ASTRI-2
ASTRI-9
Meteo-2
ASTRI-8
Data Centre

Fig. 3.2. *ASTRI Mini-array telescopes location. the red dots represent the nine telescopes [16].*

Telescope no.	Latitude	Longitude	Height[m]
1	28°18′03.69″	−16°30′28.69″	2359
2	28°18′02.43″	−16°30′23.78″	2348
3	28°18′08.52″	−16°30′29.82″	2364
4	28°18′08.31″	−16°30′23.90″	2356
5	28°18′08.73″	−16°30′17.63″	2358
6	28°18′14.92″	−16°30′24.88″	2351
7	28°18′15.56″	−16°30′18.56″	2342
8	28°17′57.45″	−16°30′31.34″	2376
9	28°18′02.75″	−16°30′33.98″	2359

Table 3.1: *ASTRI Mini-array telescopes coordinates [16]*

The environmental variables are:

- the baselines and the time delays;
- the target altitude and azimuth and expected count rates;
- the Moon altitude and azimuth and expected count rates;
- the night sky background (NSB) count rates.

This block can be divided into the functions *computeBaselines*, *checkObservability*, *computeAltAz*, *computeCountRates*, and *simulateOrbit*. Its workflow is represented in Fig. (3.3).

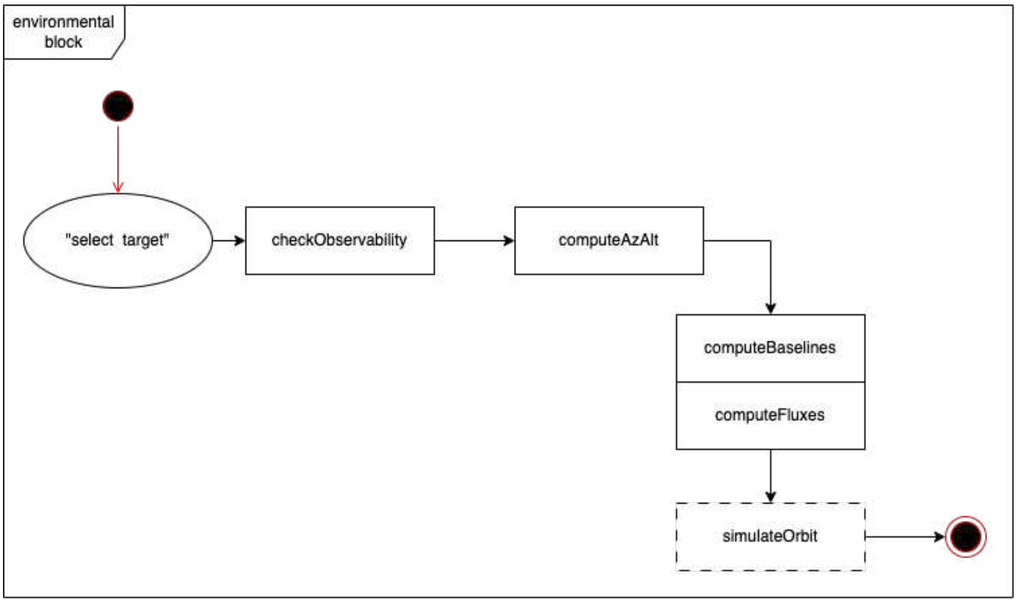

Fig. 3.3. *Environmental block workflow. First, the user selects the target, then the block sequentially executes the functions highlighted by the rectangles. The last function, simulateOrbit is only executed in the case of a binary system.*

In the following sections, each of these functions is described.

computeBaselines function

This function computes the 36 different baselines and the respective time delays of the ASTRI mini-array SI3. First, the various telescope locations are transformed into the International Terrestrial Reference System using the astropy function *EarthLocation*(). Then, the distance between each pair of telescopes is measured simply as:

$$d_{ij} = \sqrt{(x_i - x_j)^2 + (y_i - y_j)^2 + (z_i - z_j)^2}\,. \tag{3.1}$$

The distance along the line of sight can be computed with the following equation:

$$\delta_{ij} = (x_i - x_j)sin(\alpha)sin(\gamma) + (y_i - y_j)sin(\alpha)cos(\gamma) + (z_i - z_j)cos(\alpha)\,, \tag{3.2}$$

where α and γ are the target star zenith and azimuth angles respectively. The delay time is:

$$d\tau_{ij} = \delta_{ij} n_{air}/c\,, \tag{3.3}$$

where n_{air} is the air index of refraction, considered equal to 1.000293.
Finally, the baselines are:

$$b_{ij} = \sqrt{d_{ij}^2 - \delta_{ij}^2}\,. \tag{3.4}$$

Baseline computation is fundamental for any kind of interferometer. This is the vector connecting two telescopes. For an interferometer with N elements, there are $N(N-1)/2$ independent baselines.

checkObservability function

Considering that SII observations will only be carried out on full or near-full moon nights, as Cherenkov observations with such a high NSB are not possible, to simulate the data the software must first select the best nights during the year given the coordinates of the source under investigation. To this end, the *checkObservability* function checks the night of the year in which the source reaches its maximum altitude above the horizon and then looks for the nearest full Moon night. The function must then check if the Moon is at angular distances greater than 40 degrees from the target. This is needed because for smaller values the noise will be too high to perform the SII observation, as can be seen from Figure 3.4 [17] (during the full moon nights for distances from the target of less than 40-50 degrees the NSB will be much more than 20 times larger than the NSB of a moonless night). In the case of angular distances less than 40 degrees, the software thus discards the night and re-runs this check for subsequent (or previous) full moon periods until this condition is satisfied. As a final output *checkObservability* returns the dates of the 3 nights in which the observations could be performed.

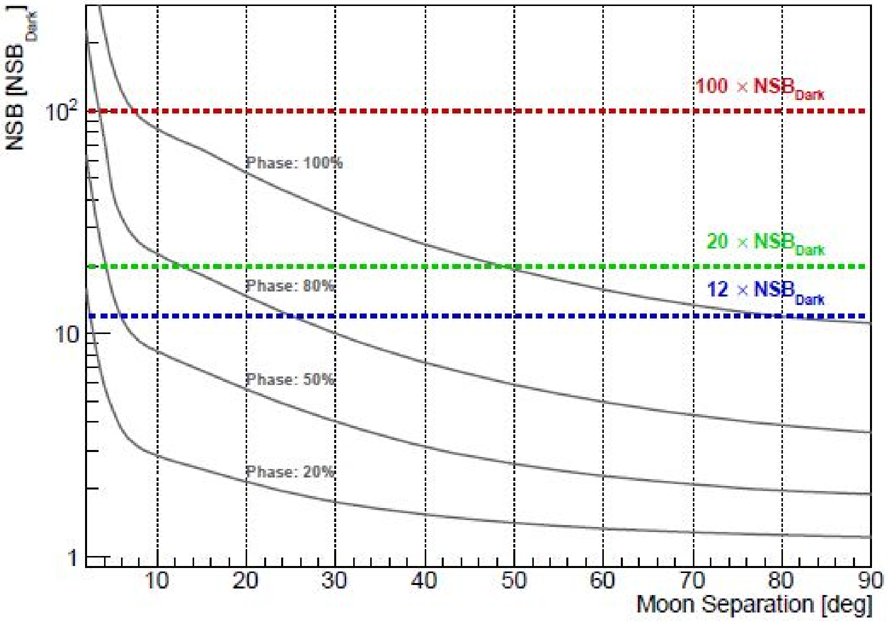

Fig. 3.4. *NSB for nights around full moon [17]. The black line represents the ratio between the NSB with the Moon in different phases and the dark NSB in function of the angular distance to the Moon. The colored dotted line represents particular NSB levels (12, 20, and 100 times the dark NSB).*

computeAltAz function

This function computes the altitude and azimuth coordinates of a celestial body. Given the time of the observations, the astropy *AltAz()* function from *SkyCoord()* converts the

Right Ascension (RA) and Declination (DEC) in altitude and azimuth.

computeCountRates **function**

This function computes the count rates of the target star background, with and without the Moon. These are obtained by first importing the star spectra according to the star type from the database developed by [18]. Then, the photon flux is computed as:

$$\Phi = 10^{-0.4m} B J_0 d\nu \,, \tag{3.5}$$

where :

- m is the star magnitude;
- B is a conversion constant, from Jy to $1/(m^2 s)$;
- J_0 is the zero point flux density in the V band, equal to 3640 Jy;
- $d\nu$ is the filter bandwidth, considered equal to 3 nm;

Then, a tophat transmission filter is applied to the photon flux, obtaining the effective star photon rate Φ in $counts/(cm^2 s)$. Finally, the count rates are estimates using the following equation:

$$ct = \Phi A \mathfrak{T} Q T_{filter} \,, \tag{3.6}$$

where :

- A is the effective area of each telescope, equal to $7m^2$;
- $\mathfrak{T}$ is the optical transmission, equal to 0.5 (this includes the reflectivity of the 3 mirrors and the focusing optics, $0.85x0.85x0.85x0.8 \sim 0.5$);
- Q is the quantum efficiency of the detector, equal to $0.5@440nm$;
- T_{filter} is the filter transmission at full width half maximum (FWHM), equal to 0.35.

Moreover, this function computes also the NSB count rate, needed to simulate the induced noise.
The NBS countrate is computed following the just explained procedure, but considering for simplicity a flat sky background spectrum with a magnitude in the V-band of ~ 21.5 per squared arcsecond (mag/arcsec^2) [24] and a detector size of 600”x600”. This value is indeed an overestimation of the possible NSB level at the site.
Other kind of noises, such as scintillations, Cherenkov effects, and other noises, have not been considered. Indeed, as explained in [7], II technique is almost insensitive to them.

simulateOrbit **function**

This function is used only for computing particular parameters when simulating binary systems. In fact, it calculates the angular separation ρ and the position angle PA given the orbital parameters of a binary system and the time of the observation.
This is done by following the procedure described by [25]. First, the eccentric anomaly, E, is computed using the function:

$$E - esinE = \frac{2\pi(t-T)}{P} \,, \tag{3.7}$$

where e is the eccentricity, t is the observation time, in Julian date, T is the periastron epoch, in Julian date, and P is the orbit period, in days. Equation (3.7) can be solved by using an iterative method. Once done this, the true anomaly, v, can be computed using the following equation:

$$tan(v/2) = \sqrt{\frac{1+e}{1-e}}tan(E/2)\,. \tag{3.8}$$

Then, the radius vector, r, is defined as:

$$r = \frac{a\left(1-e^2\right)}{1+ecosv}\,. \tag{3.9}$$

Finally, the angular separation and the position angle can be respectively computed using the following equations:

$$tan(PA-\Omega) = tan(v+\omega)cosi\,, \tag{3.10}$$

$$\rho = r\frac{cos(v+\omega)}{cos(PA-\Omega)}\,, \tag{3.11}$$

where:

- i is the orbit inclination;
- ω is the periastron argument;
- Ω is the longitude of the node.

For example, considering the orbital parameters of HD 37742 (see Table (4.3)), the apparent orbit for an entire period starting from 25/10/2023 is represented in Figure (3.5).

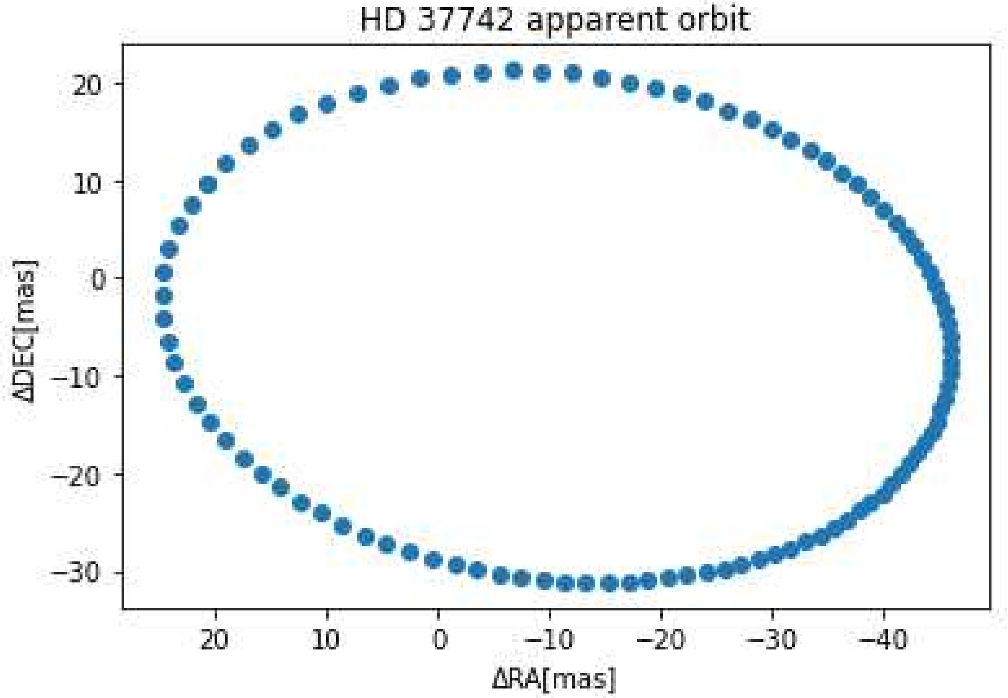

Fig. 3.5. *HD 37742 apparent orbit. This represents the motion of the secondary star around the primary one.*

3.1.2 The correlation function block

This block computes the theoretical and simulated correlation functions. The block can be divided into the following functions:

- *computeVisibility*;
- *simulateVisibility*;
- *compute2DVisibility*;
- *computeUVTracks*.

The block workflow is represented in Figure (3.6).

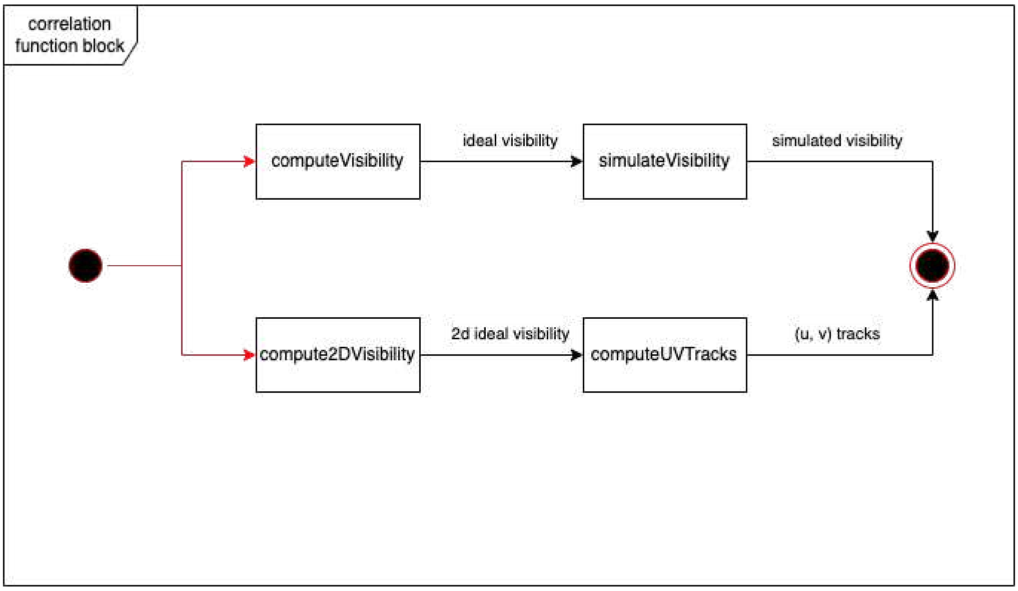
correlation function block
computeVisibility
ideal visibility
simulateVisibility
simulated visibility
compute2DVisibility
2d ideal visibility
computeUVTracks
(u, v) tracks

Fig. 3.6. *Correlation function block. This figure shows the two workflows of the block. The lower one is run in the case of a binary system.*

In the following subsections, the single functions are described.

computeVisibility function

This function computes the visibility function given a certain model for the selected target. This can be a uniform disk or a binary system. The equations have been developed referring to [19].

The visibility, μ, is related to the brightness distribution by the Van Cittert - Zernike theorem, as described in equation (1.26). Hence, for a circular uniform disk source, the visibility can be written in polar coordinates as:

$$\mu(r,\phi) = \int_0^{2\pi}\int_0^{\infty} I(\rho,\theta) exp(-2\pi i(\rho r cos(\theta-\phi))\rho d\rho d\theta\,, \qquad (3.12)$$

where ρ and θ represent the polar coordinates in the object plane, while r and ϕ represent the polar coordinates in the (u,v) plane, where u and v are spatial frequencies, or the conjugated coordinates of the spatial coordinates in the image plane. They can be computed as:

$$\rho = \sqrt{\alpha^2 + \beta^2}\,, \tag{3.13}$$

$$\theta = tan^{-1}\left(\frac{\beta}{\alpha}\right), \tag{3.14}$$

$$r = \sqrt{u^2 + v^2}\,, \tag{3.15}$$

$$\phi = tan^{-1}\left(\frac{v}{u}\right). \tag{3.16}$$

where (α,β) represents the angular coordinates on the sky, and (u, v) represents the corresponding spatial frequencies.
Equation (3.12) can be written as:

$$\mu(r) = 2\pi \int_0^\infty I(\rho) J_0(2\pi\rho r)\rho d\rho\,, \tag{3.17}$$

where J_0 is the zeroth-order Bessel function of the first kind. By representing the uniform disk source as:

$$I(\rho) = \begin{cases} 4/(\pi\theta^2) & \rho \leq \theta/2 \\ 0 & \rho > \theta/2 \end{cases}, \tag{3.18}$$

and substituting it in equation (3.17), the normalized visibility is:

$$V(u, v) = 2\frac{J_1(\pi\theta r)}{\pi\theta r}\,, \tag{3.19}$$

where J_1 is the first order Bessel function of the first kind.
In an intensity interferometer, it is measured the second order correlation function, hence, the squared visibility is equal to:

$$|V(u, v)|^2 = \left(2\frac{J_1(\pi\theta r)}{\pi\theta r}\right)^2. \tag{3.20}$$

In the uniform disk case, the PA has not been considered, being a model with radial symmetry.
For example, considering a uniform disk with an angular diameter of 0.5 mas the obtained visibility is represented in Figure (3.7).

In the case of a system with multiple bodies, the total brightness distribution can be expressed as:

$$I(\alpha,\beta) = \sum_{j=1}^{n} I_j(\alpha,\beta)\delta(\alpha - \alpha_j,\beta - \beta_j)\,, \tag{3.21}$$

where α_j and β_j represent the angular coordinates on the sky of the *j-th* body.
Then, the visibility is:

$$\mu(u, v) = \sum_{j=1}^{n} F_j V(u, v) exp(2\pi i(u\alpha_j + v\beta_j))\,, \tag{3.22}$$

and the normalized squared visibility is:

$$|V(u, v)|^2 = \frac{\sum_{j=1}^{n} F_j V(u, v) exp(2\pi i(u\alpha_j + v\beta_j))}{\sum_{j=1}^{n} F_j}. \tag{3.23}$$

In the specific case of a binary system, considering that both stars have finite size, the squared visibility can be written as:

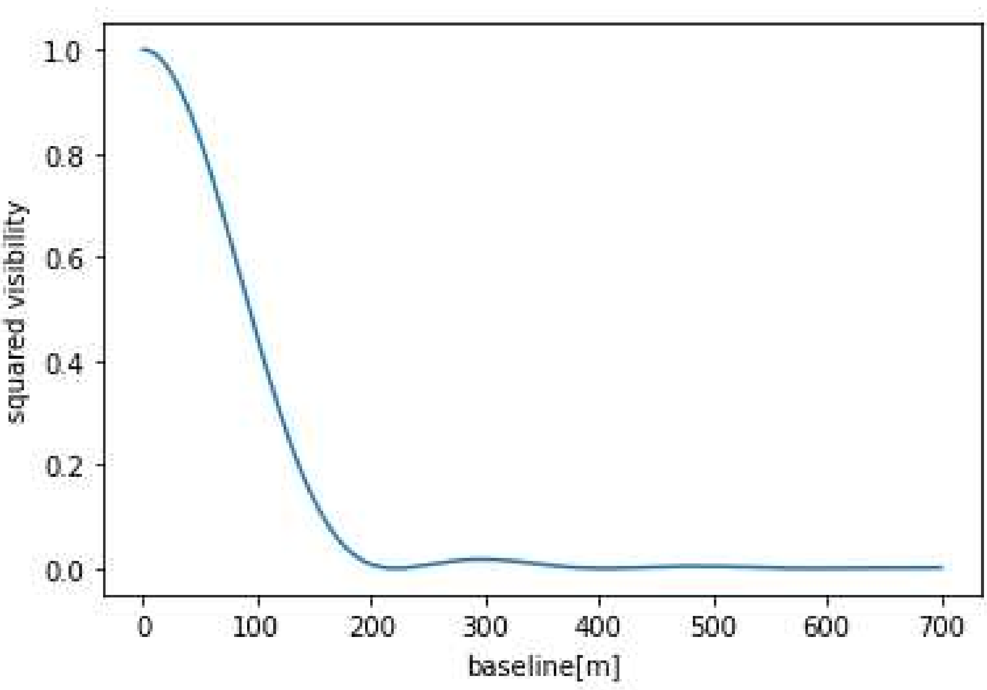

Fig. 3.7. *Ideal uniform disk squared visibility. This plot represents the second order correlation function for different baselines.*

$$|V(u,v)|^2 = \frac{V_1^2 + f^2V_2^2 + 2f|V_1||V_2|cos(2\pi/\lambda\mathbf{B}\boldsymbol{\rho})}{(1+f)^2}\,. \tag{3.24}$$

where:

- V_i is the visibility of the *i-th* star, computed with equation (3.19);
- f is the flux ratio between the two bodies,
- **B** is the baseline vector, computed as:

$$|\mathbf{B}| = \lambda\sqrt{u^2+v^2}\,; \tag{3.25}$$

- $\boldsymbol{\rho}$ is the separation vector, expressed as:

$$|\boldsymbol{\rho}| = \sqrt{(\alpha_1-\alpha_2)^2 + (\beta_1-\beta_2)^2}\,, \tag{3.26}$$

where (α_1,β_1) and (α_2,β_2) are the bodies angular coordinates.

Expanding the product $\mathbf{B}\boldsymbol{\rho}$ as:

$$\mathbf{B}\boldsymbol{\rho} = \begin{pmatrix}u\\v\end{pmatrix}\begin{pmatrix}\alpha\\\beta\end{pmatrix} = u|\boldsymbol{\rho}|sin(PA) + v|\boldsymbol{\rho}|cos(PA) = |\mathbf{B}||\boldsymbol{\rho}|(cos\phi sin(PA) + sin\phi cos(PA))\,, \tag{3.27}$$

where ϕ is defined in equation (3.16) and PA is the position angle, the visibility can be written:

$$|V(u,v)|^2 = \frac{V_1^2 + f^2V_2^2 + 2f|V_1||V_2|cos(2\pi(u|\boldsymbol{\rho}|sin(PA) + v|\boldsymbol{\rho}|cos(PA)/\lambda))}{(1+f)^2}\,. \tag{3.28}$$

Figure (3.8) represents the ideal squared visibility of a binary system with the following parameters:

- angular diameters equal to 0.5 mas;
- flux ratio equal to 0.1;
- perpendicular to the baseline;
- angular separation of 3 mas;
- λ equal to 440 nm.

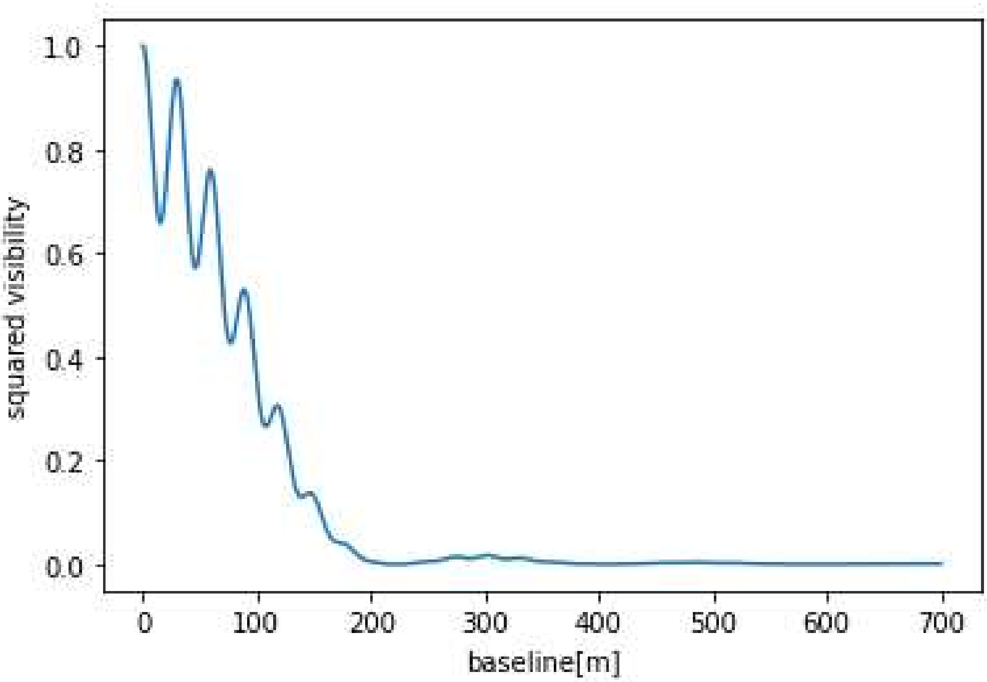

Fig. 3.8. *Ideal binary system squared visibility. It can be seen immediately how, compared to the case of a uniform disc case, represented in Figure (3.7), the presence of a secondary body induces fluctuations in the second order correlation function.*

simulateVisibility function

To simulate realistic visibility data we should define somehow the response of the instrument and determine the expected uncertainties. It is possible to do it starting from the theoretical expression of the SNR, as computed by HBT [7]:

$$SNR = \frac{\sqrt{\eta_1 \eta_2 \tau_c}\,\sqrt{T/2dt}|\gamma_{12}|^2}{(1+\alpha)}, \tag{3.29}$$

where:

- η_1 and η_2 are the photon count rates on the two detectors. These depend on the target magnitude, the target declination, the atmosphere transmittance, and the detectors' response;
- T is the integration time;
- dt is the sampling tim, in the case of SI3 it would be of the order of $\sim$ 1ns;
- $|\gamma_{12}|^2$ is the second order correlation function. This depends on the model and on the baseline between the two detectors;

- α is defined as:

$$\alpha = \frac{\sqrt{\eta_{bkg,1}\eta_{bkg,2}}}{\sqrt{\eta_1\eta_2}}\,, \tag{3.30}$$

  where $\eta_{bkg,i}$ are the background count rate on the two detectors. Essentially, α depends on the target distance from the Moon;

- τ_c is the coherence time and can be defined as:

$$\tau_c = \lambda^2/\Delta\lambda c\,, \tag{3.31}$$

  where λ is the filter central wavelength, $\Delta\lambda$ is the bandwidth of the filter in the system, and c is the speed of light.

Knowing the expected value of each measurement (from $|\gamma_{12}|^2$) and the associated uncertainty given a certain observing time from the theoretical formula of the SNR, it is possible to generate the simulated data following a Gaussian distribution. The distribution will have mean and standard deviation given by:

$$\mu_G = \frac{1}{2}|\gamma_{12}|^2\frac{\tau_c}{dt}\,; \tag{3.32}$$

$$\sigma_G = \mu_G/SNR\,, \tag{3.33}$$

considering that $SNR = \mu_G/\sigma_G$.

compute2DVisibility **function**

This function computes the ideal squared visibility of the target system on a 2D plane. This is done similarly as in the 1D case. However, in this case, the baselines are simply the points in the (u,v) plane.
Figure (3.9) represents the 2D squared visibility of HD 144217 considering a position angle equal to 75°, and a separation angle of 1.42 mas.

computeUVTracks **function**

This function computes the (u, v) tracks of the target for each baseline. These represent the spatial frequency sampling due to the Earth rotation. Following [20], the baseline vector **B** can be defined as:

$$\mathbf{B} = \lambda\begin{pmatrix} u \\ v \end{pmatrix}\,, \tag{3.34}$$

but this can also been written as:

$$\frac{\mathbf{B}}{\lambda} = \begin{pmatrix} -sin(l)sin(h) & cos(h) & cos(l)sin(h) \\ sin(l)cos(h)sin(\delta) + cos(l)cos(\delta) & sin(h)sin(\delta) & -cos(l)cos(h)sin(\delta) + sin(l)cos(\delta) \end{pmatrix}\begin{pmatrix} \Delta x_{ij} \\ \Delta y_{ij} \\ \Delta z_{ij} \end{pmatrix}\,, \tag{3.35}$$

where:

- l is the site latitude;
- h is the target hour angle;
- δ is the target declination;

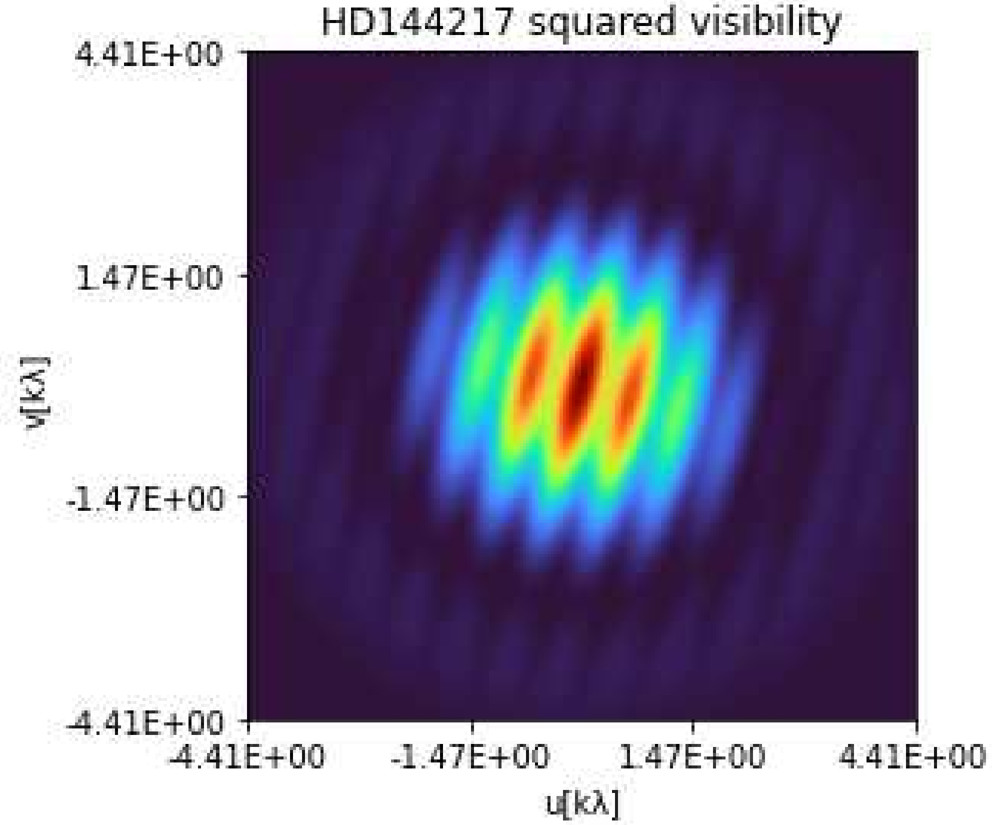

Fig. 3.9. *HD 144217 2D squared visibility. In the figure, it is clearly visible the inclination due to the PA and the fluctuations in the squared visibility due to the presence of the secondary star.*

- Δx_{ij} is the difference toward the North between the *i-th* and *j-th* telescope;
- Δy_{ij} is the difference toward the East between the *i-th* and *j-th* telescope;
- Δz_{ij} is the difference toward the Meridian between the *i-th* and *j-th* telescope.

Hence, by means of equations (3.34) and (3.35) it is possible to write:

$$u\lambda = (-sin(l)sin(h)\Delta x + cos(h)\Delta y + cos(l)sin(h)\Delta z)\,, \tag{3.36}$$

$$\begin{aligned} v\lambda &= [(sin(l)cos(h)sin(\delta) + cos(l)cos(\delta))\Delta x + \\ &+ sin(h)sin(\delta)\Delta y + (-cos(l)cos(h)sin(\delta) + sin(l)cos(\delta))\Delta z]\,. \end{aligned} \tag{3.37}$$

The just obtained equations are used to compute the (u, v) tracks given the hour angle, the target declination, and the site latitude (l = 28.301°).
An example of (u,v) tracks computed considering a target declination of -20° observed with the 9 ASTRI Mini-array telescopes for 8 hours is shown in Figure (3.10).

Once computed the (u, v) tracks and the 2D squared visibility the actual visibility measured over time from each baseline can be obtained. This is done by using the values of the (u, v) tracks as input to equation (3.28).
Considering the binary system HD 144217 at a declination of −20°, the squared visibility measured by observing with the baseline between the first and the second telescope, considering 8 hours of observation, is represented in Figure (3.11).

The corresponding observed squared visibility as a function of the hour angle (and thus of the observing time) is shown in Figure (3.12).

Finally, the obtained data to be fitted are the simulated observations along the 36 baselines, are represented in Figure (3.12).

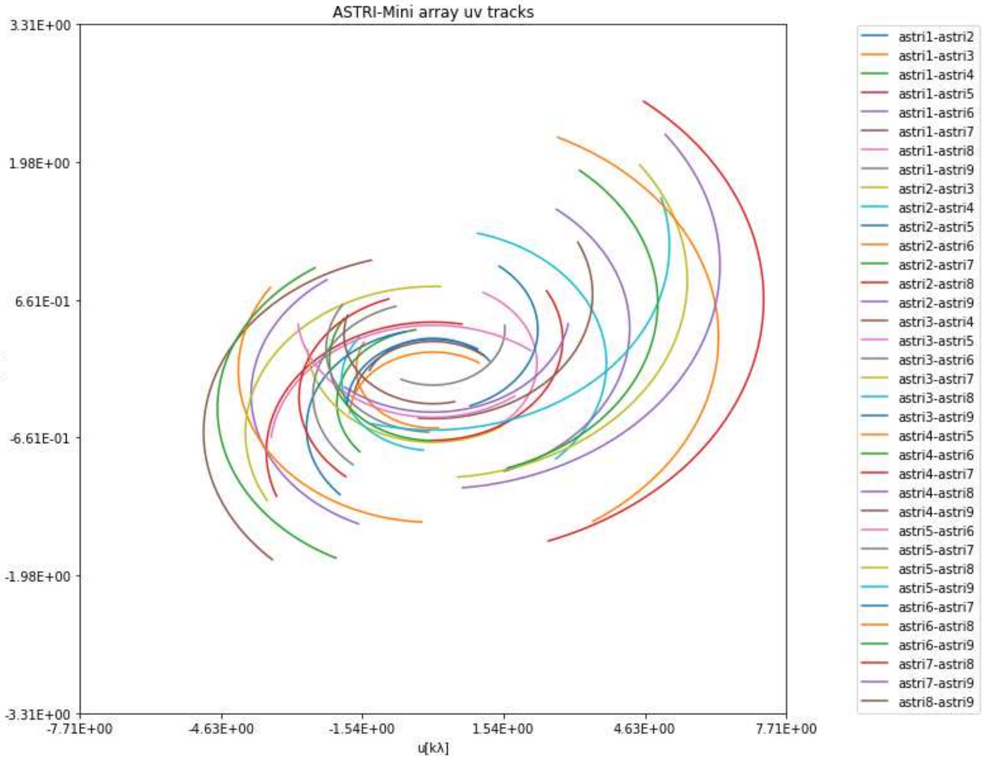

Fig. 3.10. *ASTRI Mini-array (u, v) tracks for a −20° declination target. The different colored lines represent the (u, v) track for each couple of telescopes.*

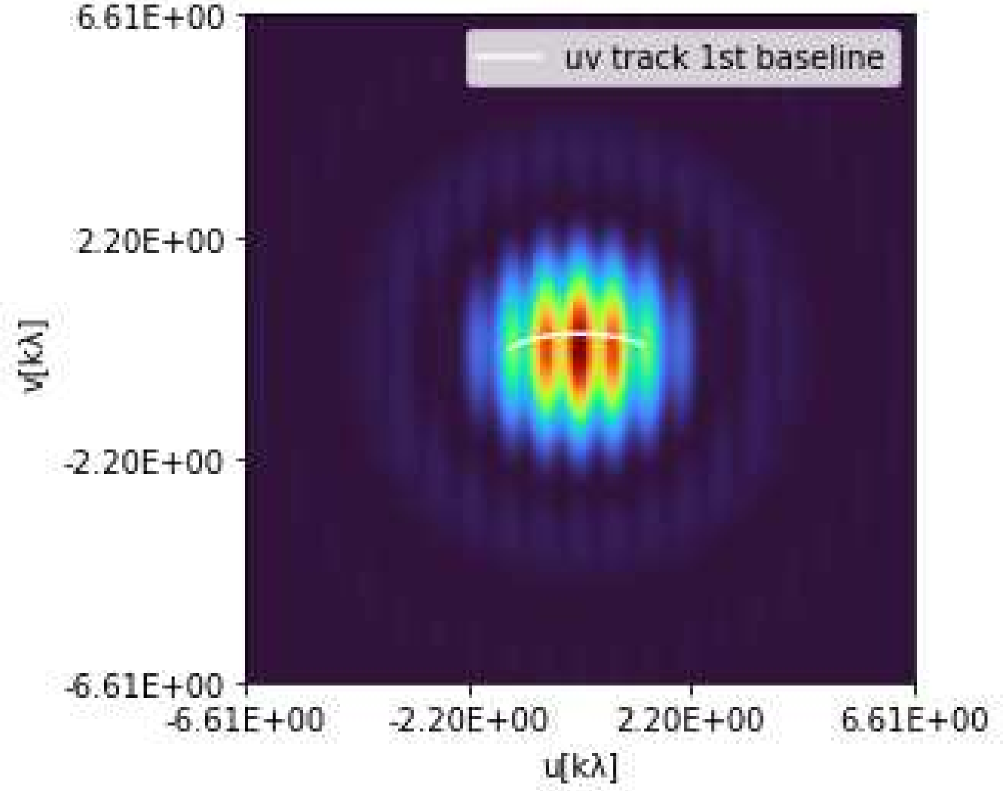

Fig. 3.11. *The white line represents the (u,v) track for a binary system at a dec −20° observed with ASTRI 1 and 2 for 8 hours, overlaid to the binary system squared visibility model.*

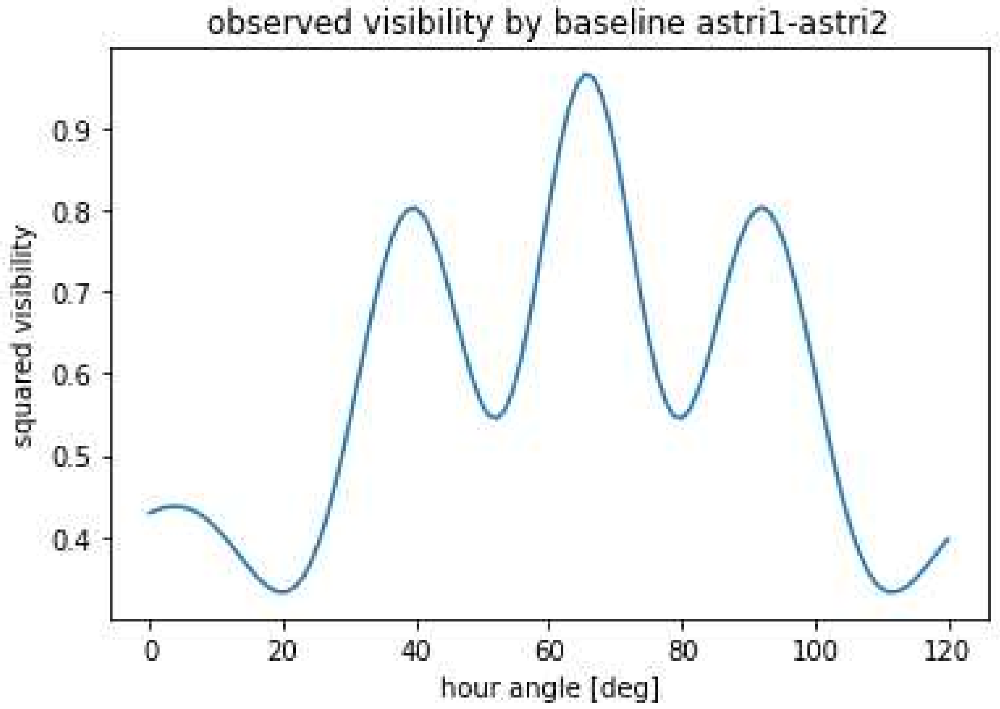

Fig. 3.12. 1^{st} *baseline measured squared visibility. This represents the squared visibility measured by the ASTRI 1 and 2 telescopes for a 8 hours observation time.*

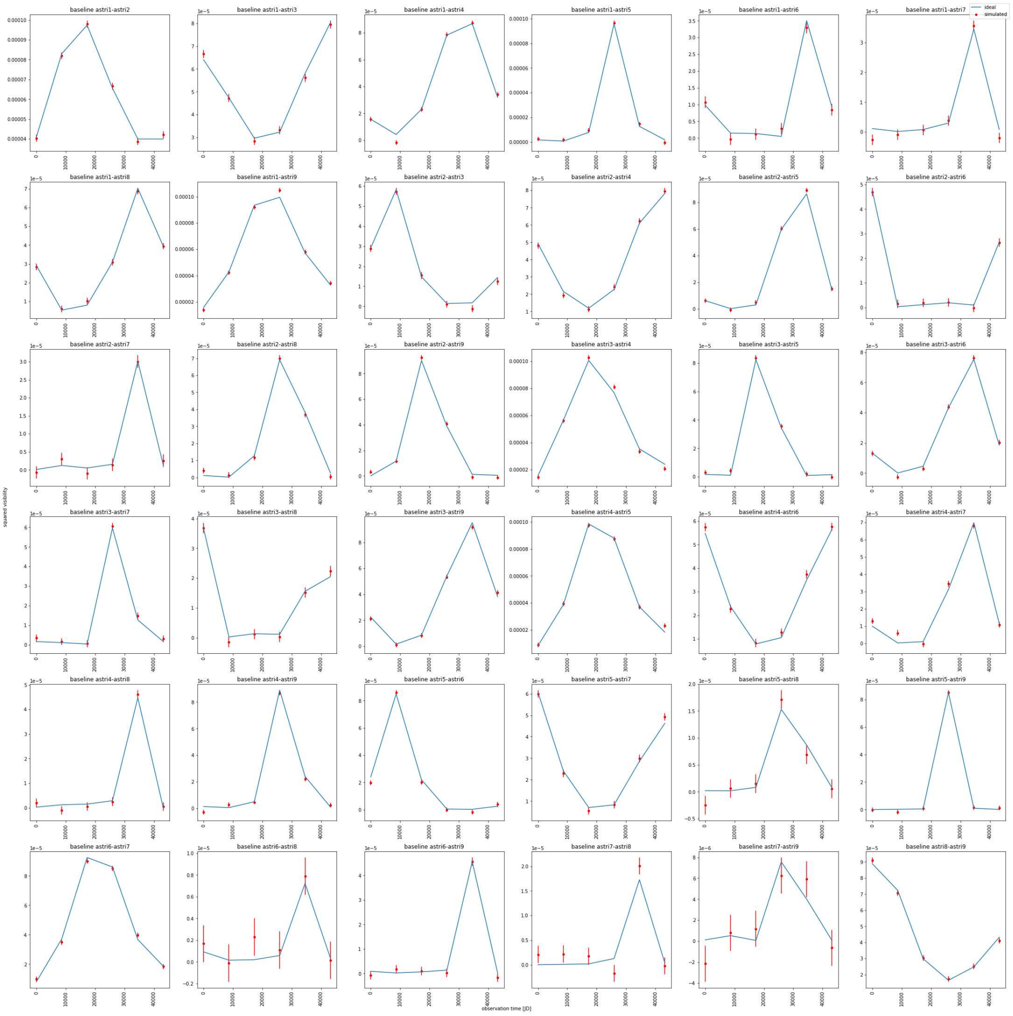

Fig. 3.13. *Baselines HD 144217 simulated observations. The red dots and their relative errors represent the observations, while the blue lines represent the ideal correlation.*

3.1.3 The fit block

These data are fitted by means of a single function, called fitData. This is represented in Figure (3.14).

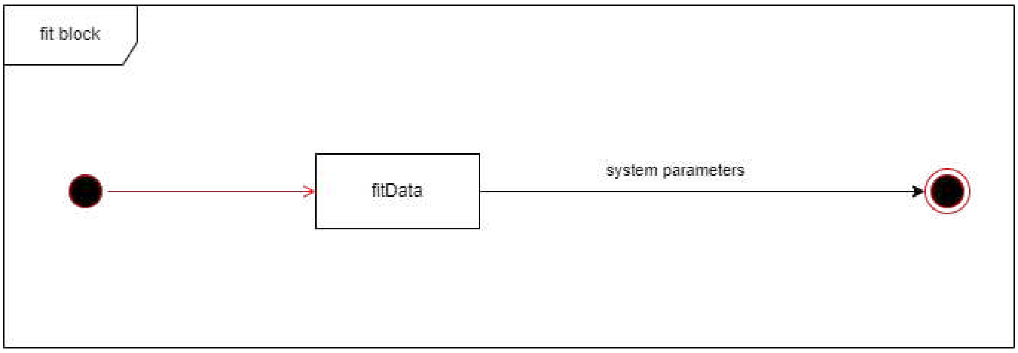

Fig. 3.14. *Fit block. This is composed by only one function.*

Initially, the Linear Least Squares (LLS) method was used to fit the data simulated with the uniform disk model, but for the binary system this method is not suitable, so a different method has been added to the software. The selected method is a Markov Chain Monte Carlo (MCMC) algorithm as implemented in python by the package *emcee* [22]. This method is based on the likelihood function optimization. The likelihood function, the probability of a dataset given the model parameters, can be written as [23]:

$$\ln p = -\frac{1}{2}\sum_n\left[\frac{\left(|V_n(u,v)|^2 - |V(u,v)|^2)^2\right)}{\sigma_n^2} + \ln\left(2\pi\sigma_n^2\right)\right], \tag{3.38}$$

where $|V_n(u,v)|^2$ are the simulated data and $|V(u,v)|^2$ the fitting model, while σ_n^2 are the error associated to each simulated measurement.
Not intending to be a comprehensive explanation of how an MCMC works, the algorithm implemented by the emcee package is explained in more detail in Appendix C.
An example of the fit for a single observation is represented in Figure (3.15).

In the fitting procedure of the angular diameters of the two stars in a binary model, it is taken into account that these measurements are made every few hours. This results in multiple measurements of the diameters, together with the relative positions of the stars, as will be seen in the next chapter. The final angular diameters are then obtained with a weighted average of the fitted diameters using the following equation:

$$\overline{x} = \frac{\sum_{i=1}^{n}(x_i w_i)}{\sum_{i=1}^{n} w_i}, \tag{3.39}$$

where w_i are the weights, computed as the reciprocal of the variance:

$$w_i = \frac{1}{\sigma_1^2}, \tag{3.40}$$

while its error is computed as:

$$\sigma_{\overline{x}} = \sqrt{\frac{1}{\sum_{i=1}^{n} w_i}}. \tag{3.41}$$

Figure (3.16) represents the parameters covariance of a single three hours observation fit.

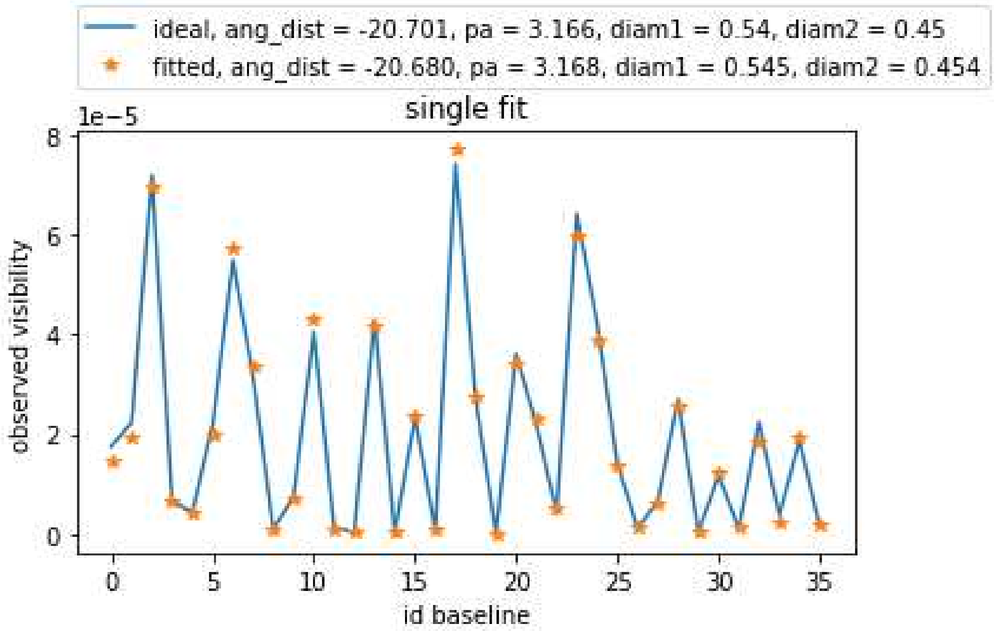

Fig. 3.15. *Single observation fit. The orange dots represent the fitted points, while the blue line represents the ideal correlation. In the upper legend, the ideal and the fitted results are reported.*

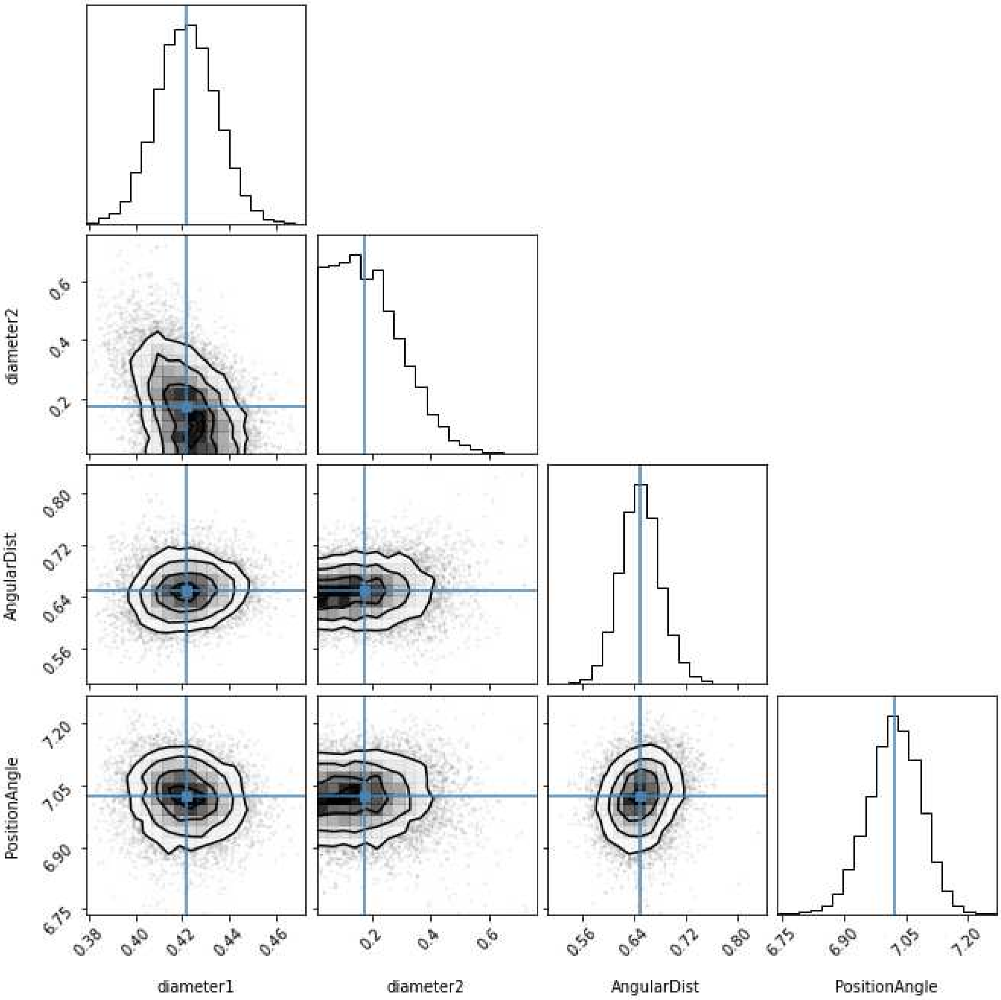

Fig. 3.16. *Parameters covariance for a three hours observation. Each one- and two-dimensional projection of the sample represents the covariances of the fitted parameters.*

While the fitted positions on the sky for the secondary component (the primary is considered to be fixed at $x = 0$ and $y = 0$) can be expressed as:

$$x = \rho sin(PA)\,; \tag{3.42}$$
$$y = \rho cos(PA)\,, \tag{3.43}$$

and their relative errors are computed following the error propagation formula as::

$$\sigma_x = \sqrt{|sin(PA)|\sigma_\rho^2 + |\rho cos(PA)|\sigma_{PA}^2}\,; \tag{3.44}$$
$$\sigma_y = \sqrt{|cos(PA)|\sigma_\rho^2 + |\rho sin(PA)|\sigma_{PA}^2}\,, \tag{3.45}$$

where σ_{PA} and σ_ρ are the errors extracted from the fitting procedure on the position angle and on the angular separation respectively. When propagating the errors, the covariance terms between ρ and PA have been considered negligible since only a very small correlation is found between these two parameters.

Chapter 4

Results

In this chapter, the results from the simulations made with the software described in the previous chapter, are presented and commented on.
In the first section, a brief analysis of the simulations performed with the uniform disk model will be presented in order to understand which characteristics are most suitable for a star that can be studied with the ASTRI Mini-Array. In the second section, the simulations carried out with the binary system model will be analyzed, taking various systems into consideration and evaluating which of them are suitable for more in-depth studies.

4.1 Uniform disk simulation

As a first analysis, the capabilities of ASTRI Mini-array in characterizing ideal stars (i.e. with a uniform irradiance and a radial symmetry) under varying parameters were studied.
The parameters to be varied are the angular diameters and fluxes of some ideal stars. In this way, we can map the parameter space and find the optimal ranges within which the Mini-array can work.
To do so, however, a number of other parameters must be fixed so that a meaningful comparison can be made. The fixed parameters are:

- the zenith angle equal to 60°;
- the azimuth angle equal to 30°;
- the central wavelength equal to 440 nm with a bandwidth of 3 nm;
- a sampling time of 1 ns;
- a total observing time of 8 hours.

These analyses did not have the objective of defining the tolerances and observability limits of the system. However, they can be useful for understanding the main measurement dependencies.

4.1.1 Variable diameters

This analysis considers as a reference a $B0$ type star with a fixed magnitude of 2. The following angular diameters were analyzed: 0.1 mas, 0.5 mas, 1 mas, 3 mas, and 10 mas. The NSB is computed as explained in the *computeCountRates()* function section. By looking at equation (3.19), it is expected that the resulting visibility spreading would decrease as the diameter increases. Given the average baselines of the ASTRI Mini-array (between 100 and 700 meters), it is clear that the best performances can be obtained for quite small targets (below 500 mas) as can be seen from Figure (4.1).

Therefore, to get an estimate of the performance of the LLS fit implemented in the software, as the angular diameter varies, a Markov Chain Monte Carlo (MCMC) analysis is carried out with 1000 samples (for each angular diameter studied). The results obtained are then fitted with a Gaussian curve to extract the average value and the standard deviation. As an example, in Figure (4.2) the results of the analysis for a diameter of 0.5 mas are represented.

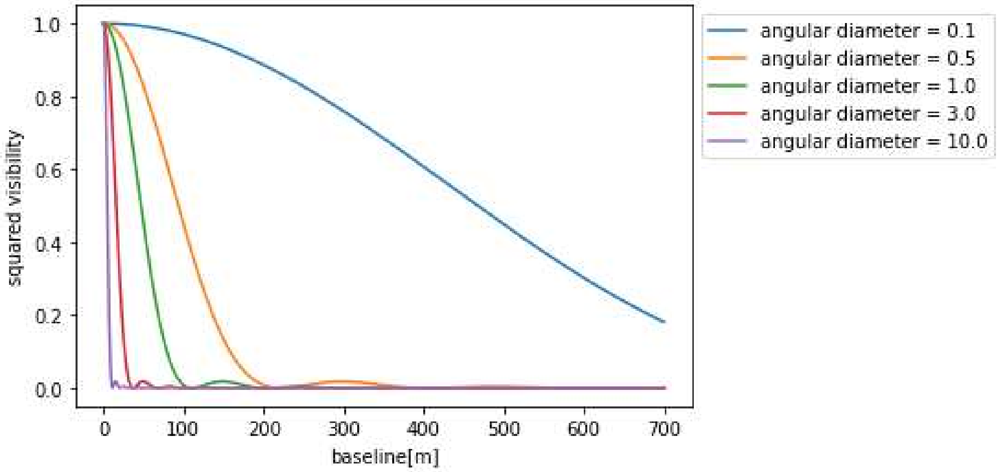

Fig. 4.1. *Ideal uniform disks squared visibility with variable angular diameter. As the diameter increases, squared visibility narrows.*

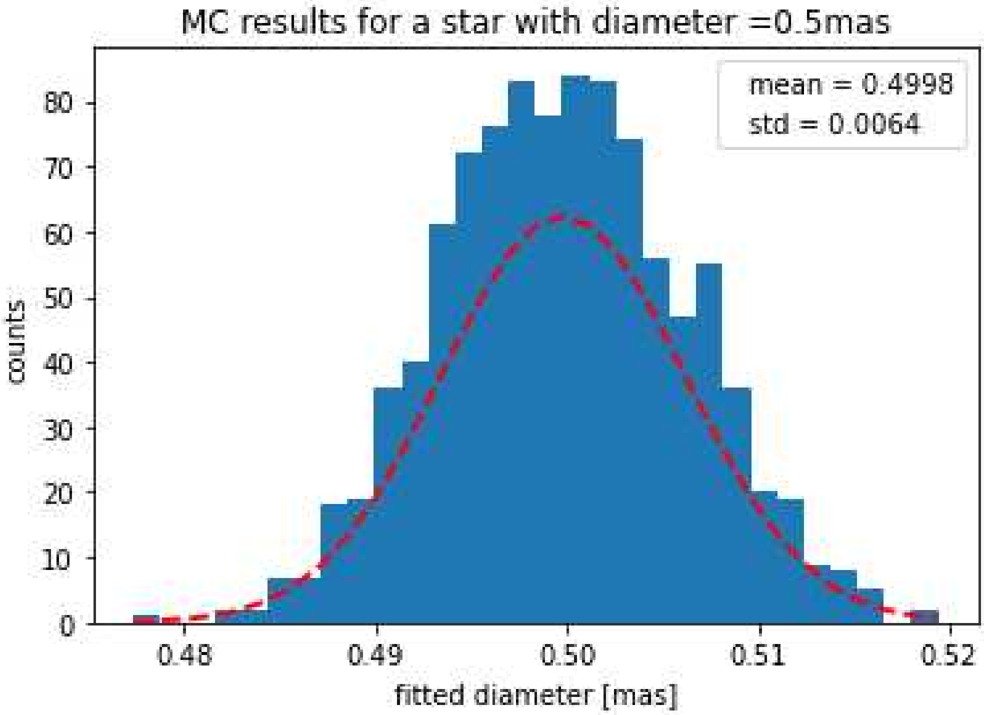

Fig. 4.2. *MC results fitting a 0.5 mas uniform disk. The dotted red line represents the Gaussian fit, while the blue histogram represents the LLS fit results.*

The final error can be computed as:

$$\epsilon = \frac{|x - \mu|}{x}, \tag{4.1}$$

where x is the simulated diameter, and μ is the fitted diameter measured from the Gaussian distribution.

The fit performance is reported in Table (4.1).

Secondary diameter [mas]	Relative error [%]
0.1	0.1
0.5	0.1
1	21.5
3	17.8
10	66.8

Table 4.1: *Fit performance for variable diameters.*

For diameters larger than ~500 mas, the visibility becomes much narrower and the baselines will only cover the part of the visibility that is almost constantly zero, making it more difficult to fit the diameter of the stars.

4.1.2 Variable star fluxes

The same procedure was followed in analyzing a variable magnitude. This was simulated by varying the star magnitude and spectral type while keeping the angular diameter fixed, which was set equal to 0.5 mas. The following magnitude values were simulated:

- $A1$ type star, with magnitude equal to -1.46;
- $B1$ type star, with magnitude equal to 0.97;
- $B8$ type star, with magnitude equal to 2.06;
- $M5$ type star, with magnitude equal to 3.06;
- $K3$ type star, with magnitude equal to 4.

By looking at equation (3.29), the SNR is expected to increase with increasing photon flux, while the correlation function does not change. Finally, the performance of the fit is represented in Table (4.2).

As expected, the accuracy of the fit decreases with increasing magnitude. A more detailed study on how performance changes as parameters vary in the two-telescope scenario can be found in [26].

4.2 Binary system preliminary simulations

As in the case of a uniform disk source, at the beginning of the analysis, the visibility dependence on various parameters was investigated. In this way, it is possible to understand how the visibility curve changes changing these parameters: the angular diameters of the stars in the binary system, the flux ratio between the two stars, the position angle at the time of the observation, and the angular separation at the time of the observation. Instead, the following parameters are assumed constant:

Star magnitude	Relative error [%]
-1.46	0.1
0.97	0.1
2.06	4.7
3.06	59.5
4	68.1

Table 4.2: *Fit performance for variable fluxes.*

- the zenith angle equal to 60°;
- the azimuth angle equal to 30°;
- the central wavelength equal to 440 nm with a bandwidth of 3 nm;
- a sampling time of 1 ns;
- a $B0$ type star with magnitude equal to 2;
- an observing time of 8 hours.

The NSB is computed as explained in the *computeCountRates()* function section.
It was chosen to keep the angular diameter of the primary fixed as we are interested in understanding how the introduction of a companion star perturbs the squared visibility of the main body. Furthermore, considering the diameter of the primary star as the largest, the effect of the secondary body, as will be seen in the following analysis, is a modulation of the visibility of the primary body alone.

4.2.1 Variable diameters

This analysis makes varying the secondary diameter, assuming the following values: 0.10 mas, 0.82 mas, 1.55 mas, 2.27 mas, and 3.00 mas.
Instead, the following values were assumed to be constant: primary diameter: PA equal to 90°, flux ratio equal to 0.1, ϕ equal to 0°, and ρ equal to 3 mas.
The obtained squared visibilities are shown in Figure (4.3).

4.2.2 Variable flux ratio

This analysis makes varying the flux ratio, assuming the following values: 0.0100, 0.2575, 0.5050, 0.7525, and 1.0000.
Instead, the following values were maintained constant: secondary diameter equal to 0.5 mas, PA equal to 90°, ϕ equal to 0°, and ρ equal to 3 mas.
The obtained squared visibilities are represented in Figure (4.4).

4.2.3 Variable position angle

This analysis makes varying the position angle, assuming the following values: 0.0°, 22.5°, 45.0°, 67.5°, and 90.0°.
Instead, the following values were maintained constant: secondary diameter equal to 0.5 mas, flux ratio equal 0.1, ϕ equal to 0°, and ρ equal to 3 mas.
The obtained squared visibilities are represented in Figure (4.5).

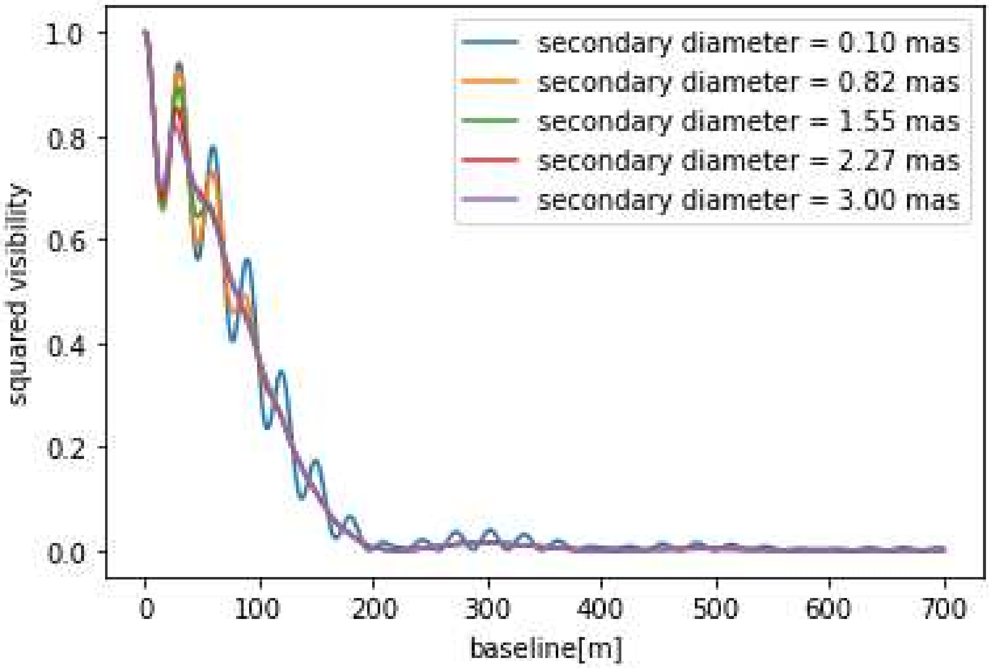

Fig. 4.3. *Binary system squared visibility with variable secondary body diameter. The various colored lines represent various binary system models with different secondary diameter values. The smaller the diameter of the secondary star, the larger the modulation remains even at large baselines. For sufficiently large diameters of the secondary (much larger than the primary star), the modulation is instead only visible at the smallest baselines.*

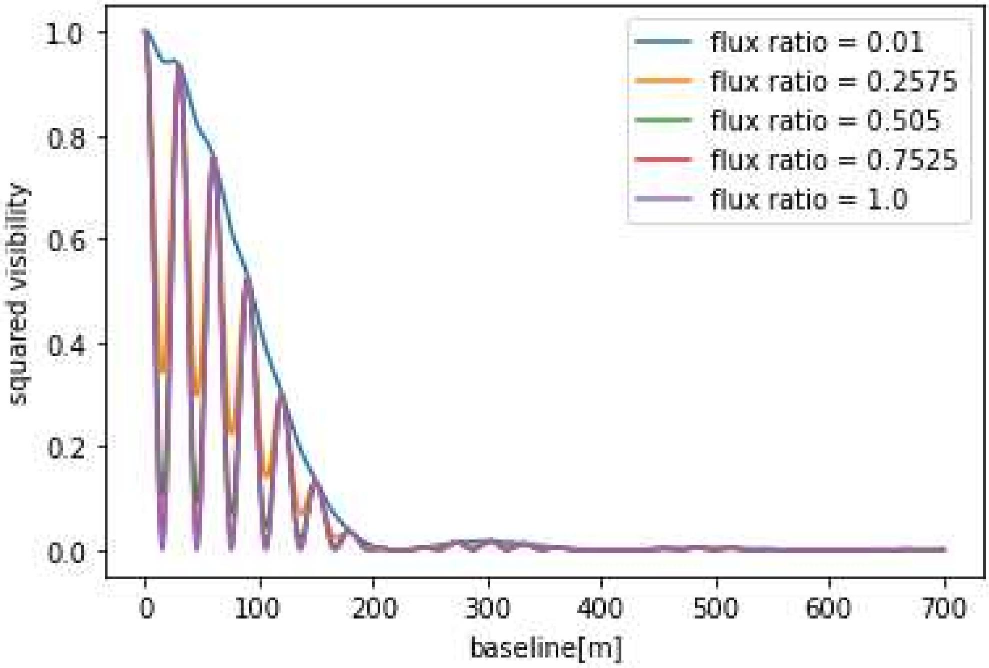

Fig. 4.4. *Binary system squared visibility with variable flux ratio. The various colored lines represent various binary system models with different flux ratio values. The larger the flux ratio, the larger the squared visibility fluctuations. In all the cases, however, the visibility that would be obtained from the primary body alone is modulated.*

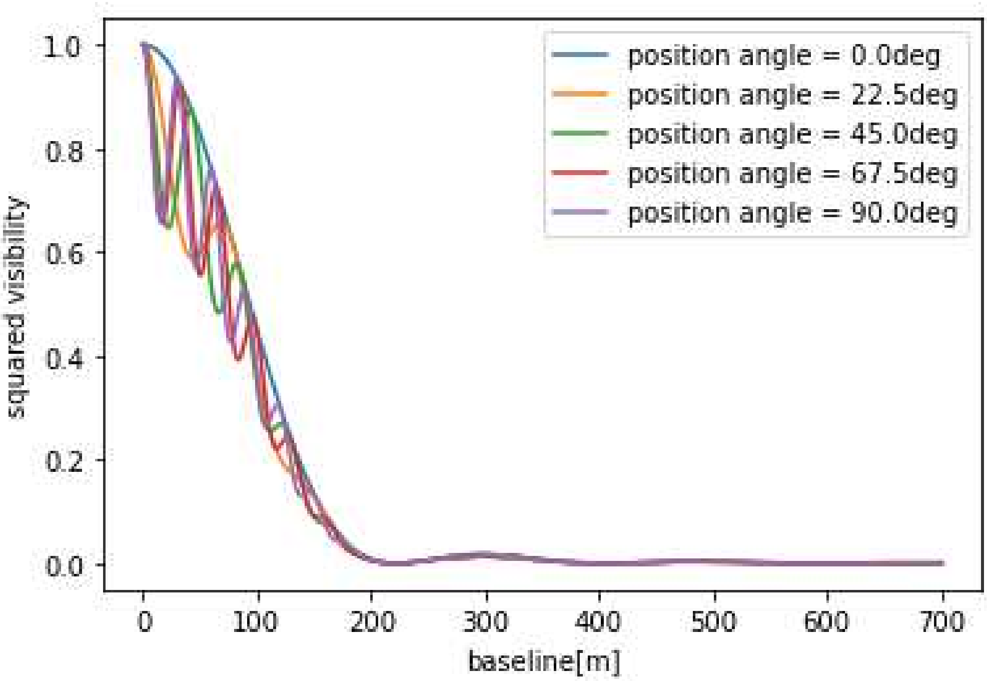

Fig. 4.5. *Binary system squared visibility with variable PA. The various colored lines represent various binary system models with different PA values. For a PA equal to the baseline orientation ($PA = \phi = 0°[\pm180°]$) the squared visibility is equivalent to that obtained for a single star. In contrast, in the case of a PA perpendicular to the baseline orientation ($PA = \phi = 90°[\pm180°]$) the fluctuations reach maximum levels. For all the situations in between, the fluctuation tends to disappear as the PA tends to zero.*

4.2.4 Variable angular separation

This analysis makes varying the angular separation, assuming the following values: 1.00 mas, 1.75 mas, 2.50 mas, 3.25 mas, and 4.00 mas.
Instead, the following values were maintained constant: secondary diameter equal to 0.5 mas, flux ratio equal to 0.1, PA equal to 90°, and ϕ equal to 0°.
The obtained squared visibilities are represented in Figure (4.6).

4.3 Selected binary systems

Through a search in the literature, a preselection was made of the potential binary systems that might have the right characteristics to be studied with the ASTRI Mini-array. The main criteria used for the pre-selection of the binary system were the total brightness of the systems (magnitude < 5) and the angular size of the main component (< 600 mas). The selected systems are: HD 37742, HD 144217, and HD 24912.
The flux ratio, when the two stars magnitude were found, has been computed using the following equation [27]:

$$f = 2.512^{\Delta m}, \tag{4.2}$$

where Δm is the two stars magnitude difference in the B band. In the case the magnitude difference between the two bodies in the binary system is not known through spectroscopic or photometric studies, an iterative approach can be used by varying the flux ratio initial guess in the *emcee* fit until the result agrees with the orbital parameters measured by spectroscopy. It is certainly a time-consuming and expensive method, but it would allow the flux ratio between the two bodies to be measured.
In the following tables, the orbital parameters of the various systems are reported.

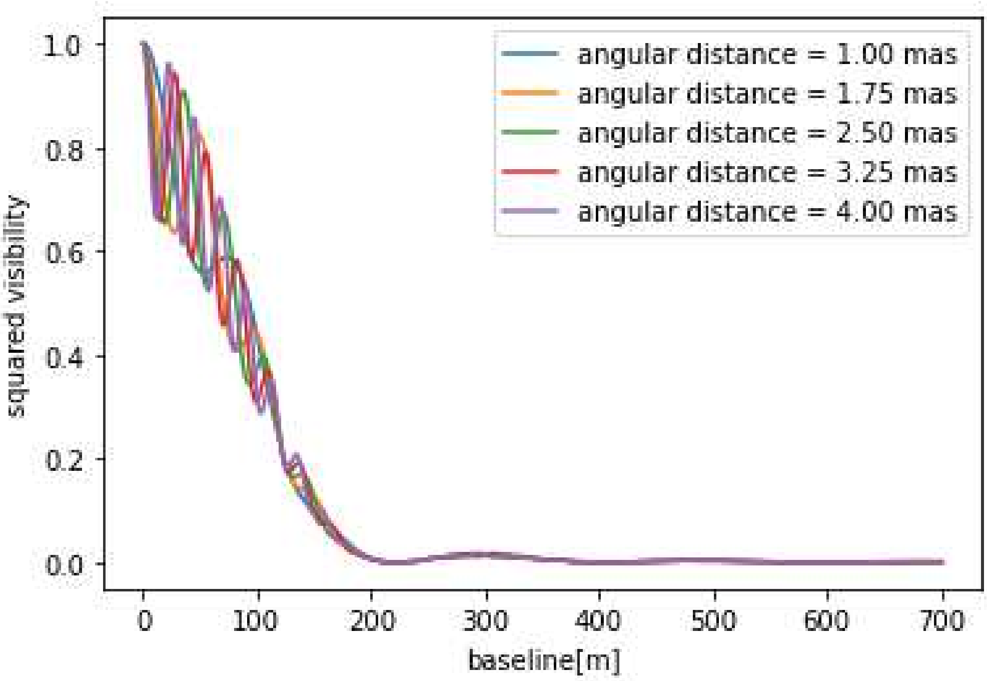

Fig. 4.6. *Binary system squared visibility with variable angular separation. The various colored lines represent various binary system models with different angular separation values. The larger the distance, the higher will be the frequency of the modulation, while the amplitude of this modulation seems to be unaffected by this parameter. This also means that for very large distances between the two stars, the frequency will be so high that it will actually not be easy to measure.*

4.3.1 HD 37742

HD 37742 is part of a triple star system called Alnitak. The system is located in the constellation of Orion. In this thesis, the binary system consisting of ζ Ori Aa and ζ Ori Ab was considered. ζ Ori Aa is a blue supergiant of spectral type O9.5Iab, while ζ Ori Ab is a blue subgiant of spectral type B1IV [28].
Table (4.3) reports the orbital parameters of HD 37742.

4.3.2 HD 144217

HD 144217 is a component of the multiple star system named β Scorpii, located in the southern zodiac constellation of Scorpius. At present, the system is thought to consist of 6 stars. Of these we are interested in the binary system consisting of β Sco Aa and β Sco Ab. These are the most massive members of the system, and their respective spectral types are estimated to be B0.5 and B1.5 [31].
Table (4.4) reports the orbital parameters of HD 144217.

4.3.3 HD 24912

HD 24912, also called ζ Persei, is a star in the northern constellation of Perseus. HD 24912, according to [35], is classified as a lower luminosity B1 Ib supergiant star.
Table (4.5) reports the orbital parameters of HD 24912.

In this particular case, no data regarding the orbital parameters and the secondary star diameter have been found. Following a conservative approach, a secondary diameter of 0.15 mas was considered. Moreover, in [36], HD 24912 is considered as a runaway star. According to [37] these kind of stars are usually single, so the literature results can be due to a unspecified type of photospheric variability.

HD 37742	
Binary system WDS identifier	$J05407 - 0157Aa, Ab$
Semimajor axis[29]	35.9 ± 0.2 mas
Eccentricity[29]	0.338 ± 0.004
Inclination[29]	139.3 ± 0.6°
Angular diameters[30]	0.54 ± 0.01 mas - 0.45 ± 0.12 mas
B magnitudes[34]	$1.797 - 3.553$
Flux ratio	0.1984
Period [29]	2687.3 ± 7.0days
Longitude of the node [29]	83.8 ± 0.8°
Periastron epoch [29]	2452734.2 ± 9.0 JD
Argument of periastron [29]	24.2 ± 1.2°

Table 4.3: *HD 37742 binary system parameters found in the literature.*

HD 144217	
Binary system WDS identifier	$J16054 - 1948AB$
Semimajor axis[31]	1.42 ± 0.02 mas
Eccentricity[31]	0.291 ± 006
Inclination[31]	111.8 ± 0.7°
Angular diameters[32]	0.422±0.026 mas - 0.264±0.019 mas
B magnitudes[34]	$2.546 - 4.789$
Flux ratio	0.1267
Period [33]	6.828245 days
Longitude of the node [33]	294.2 ± 0.8°
Periastron epoch [33]	2449788.509 ± 0.019 JD
Argument of periastron [33]	54.8 ± 1.3°

Table 4.4: *HD 144217 binary system parameters found in the literature.*

HD 24912	
Binary system WDS identifier	$J03590+3547AB$
Semimajor axis[36]	$2.4''$
Angular diameters[36]	0.216 ± 0.016 mas - ?
B magnitudes[34]	$4.026-13.826$
Flux ratio[36]	0.0001

Table 4.5: *HD 24912 binary system parameters found in the literature.*

4.3.4 Binary systems preliminary analysis

Investigating the orbital parameters of the various systems, HD 24912 is expected to have a flux ratio too small to be distinguishable from a uniform disc. Furthermore, the angular separation of HD 37742 is very high, causing large fluctuations in the squared visibility. The values of HD 144217, on the other hand, seem to make it suitable to be characterized by ASTRI. All these considerations are taken up in the next analyses.
In the next sections, the different systems squared visibilities were compared to a uniform disk squared visibility, to verify their actual difference from a simple one-body model.
The following parameters were considered: PA equal to 90°, and ϕ equal to 0°.

HD 144217 Analysis

In Figure (4.7) it is represented the comparisons between HD 144217 squared visibility in case of a binary system with the parameters reported in Table (4.4) and the following uniform disk diameters: 0.4 mas, 0.5 mas, and 0.6 mas.

From the difference depicted in Figure (4.7) it is clear how the binary squared visibility is well distinguishable against any kind of uniform disk.
Moreover, this system is quite close, around 300 mas, to another star whose magnitude is 5.856 [38], and whose angular diameter has not been found in the literature. This has been considered equal to 0.21 mas. To quantify the extent to which this third star can actually generate a measurable contribution, a 2D model of the sky brightness distribution of the 3-stars system was implemented, and by directly applying the Van Cittert-Zernike theorem, the squared visibility to compare with the simple binary system case was obtained via a Fourier transform. The two obtained squared visibilities are shown in Figure (4.8). The two models are practically indistinguishable, apart from some minor differences that will not actually be measurable. This is basically due to the fact that the flux of the third star is much smaller than the other components of the system and justifies the simplification of considering only the two brightest components in the subsequent analysis.

HD 37742 Analysis

In Figure (4.9) it is represented the comparisons between HD 37742 squared visibility and the following uniform disk diameters: 0.6 mas, 0.7 mas, and 0.8 mas.

From the difference depicted in Figure (4.9) it is clear how the binary squared visibility is well distinguishable against any kind of uniform disk. However, due to the wide fluctuations in visibility, one would have expected a poor fit performance. This was positively refuted in the following sections. In fact, the fluctuations decrease with the PA.

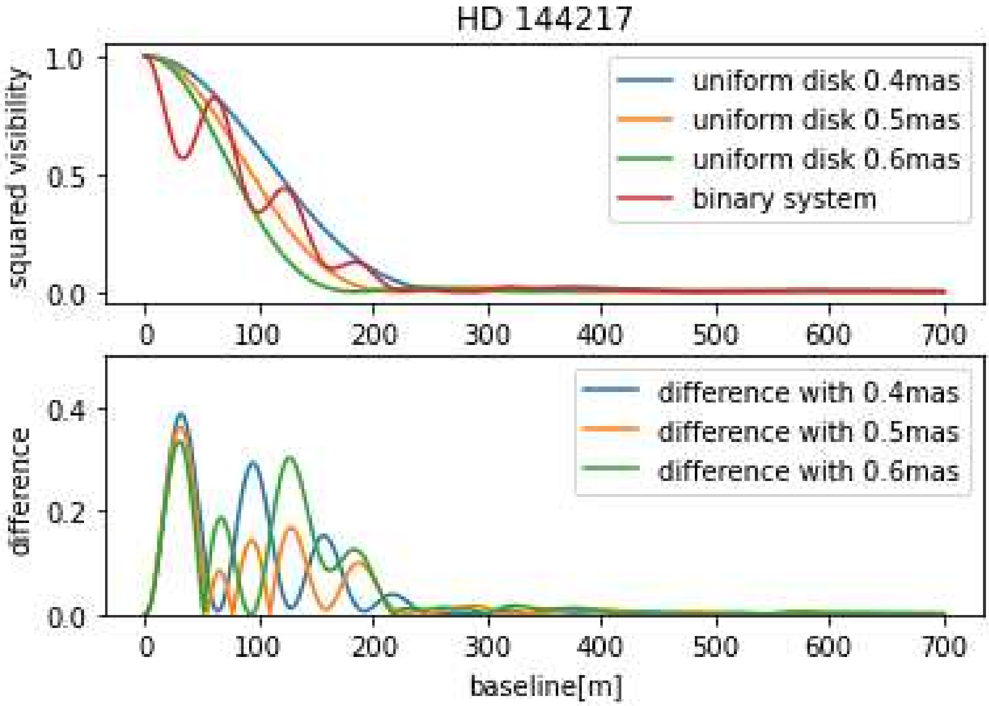

Fig. 4.7. *HD 144217 squared visibility vs uniform disk squared visibilities. The upper figure represents the squared visibilities for the various cases. The blue line represents the binary system, while the other colors represent the uniform disk cases. The lower figure represents the differences between the binary system squared visibility and the uniform disk ones.*

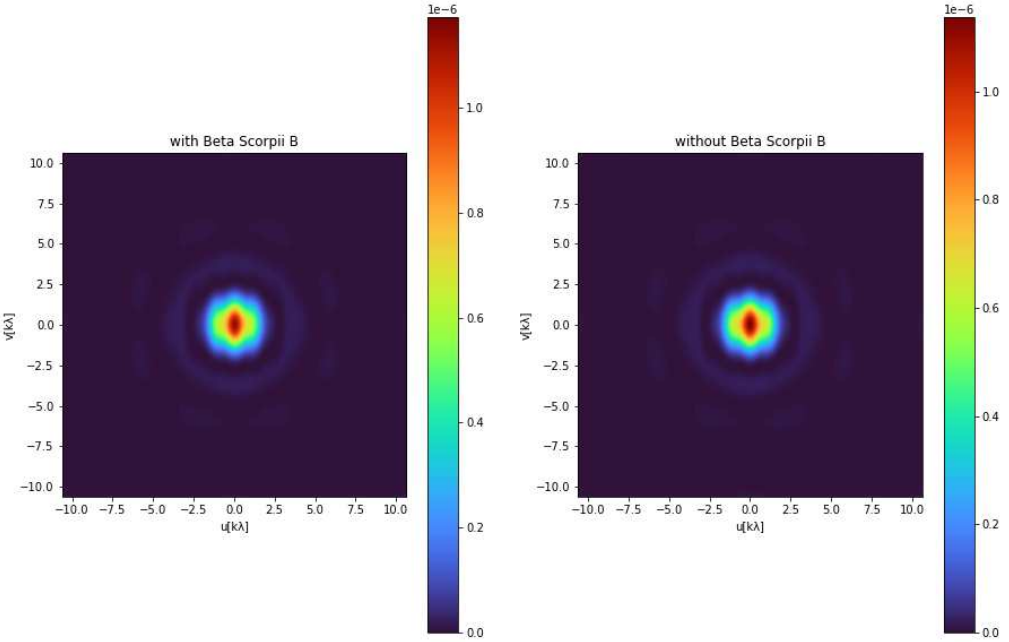

Fig. 4.8. *Fourier analysis on Beta Scorpii B disturbance. Two squared visibilities are represented, on the left the one obtained considering also the third star, and on the right the one obtained without it.*

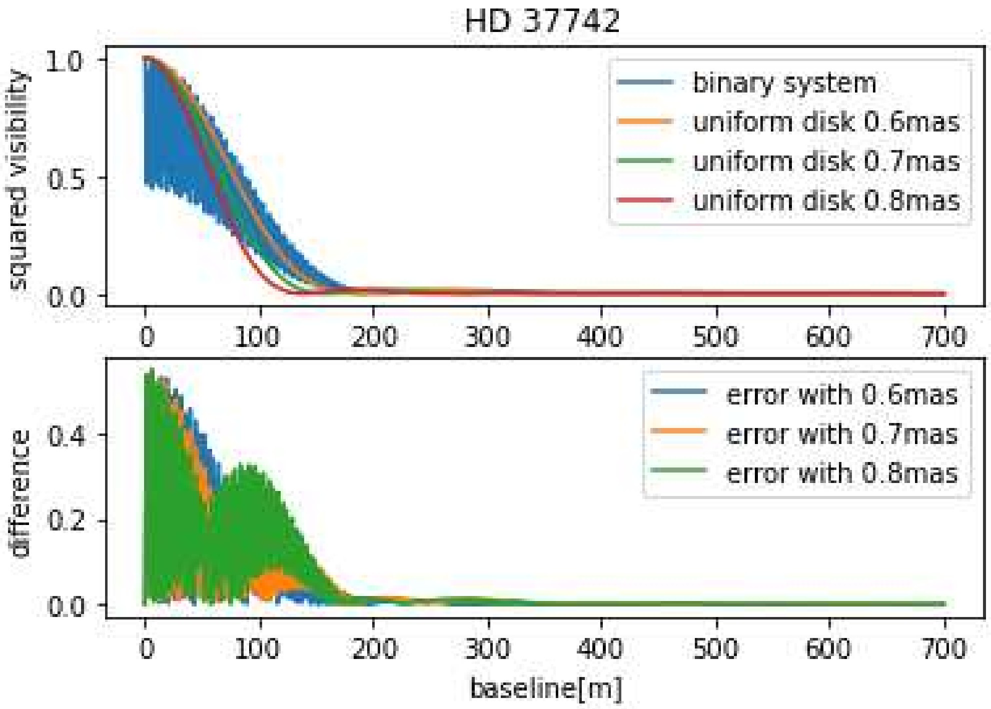

Fig. 4.9. *HD 37742 squared visibility vs uniform disk squared visibilities. The upper figure represents the squared visibilities for the various cases. The blue line represents the binary system, while the other colors represent the uniform disk cases. The lower figure represents the differences between the binary system squared visibility and the uniform disk ones.*

Since ζ Ori B is about 3’ apart from the investigated binary system [28], it is expected that this does not affect the binary system squared visibility, also considering the results obtained when including the third component for HD 144217.

HD 24912 Analysis

In Figure (4.10) it is represented the comparisons between HD 24912 squared visibility and the following uniform disk diameters: 0.2 mas, 0.22 mas, and 0.25 mas.

From the difference depicted in Figure (4.10) it is clear how the binary squared visibility cannot be distinguished from a uniform disk. This is due to the low flux ratio between the two stars.

4.4 HD 144217 characterization

Following the results shown in the previous sub-section, it was decided to proceed with a more in-depth analysis of the binary system that gave the most promising results, namely HD 144217.
Firstly, the best period for the observations was chosen following a slightly modified procedure with respect to the one described in section 3.1.1 (to maximize the observing hours the constraints on the full Moon were removed). The best period is shown in Figure (4.11).

hence, 20/05/2025 is selected as the night of observation.
It was decided to simulate one observation every three hours, as the orbital period is very short (only 6 days). Then, the ideal and simulated observations for the various baselines along five consecutive observation nights are shown in Figure (4.12). These were computed following the procedure described in section (3.1.3).

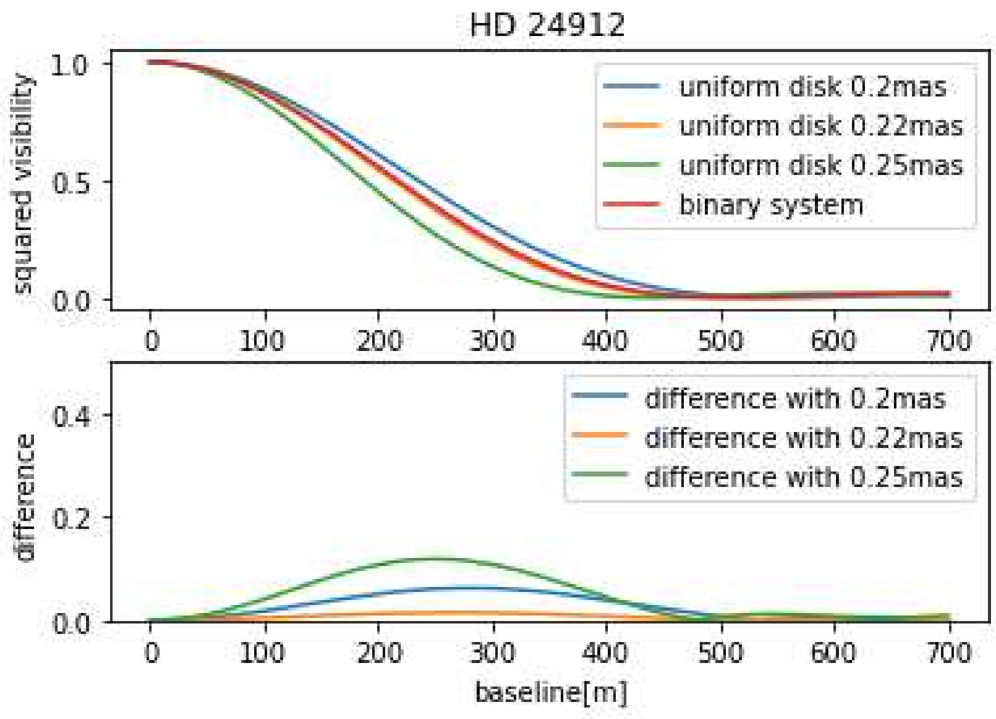

Fig. 4.10. *HD 24912 squared visibility vs uniform disk squared visibilities. The upper figure represents the squared visibilities for the various cases. The blue line represents the binary system, while the other colors represent the uniform disk cases. The lower figure represents the differences between the binary system squared visibility and the uniform disk ones.*

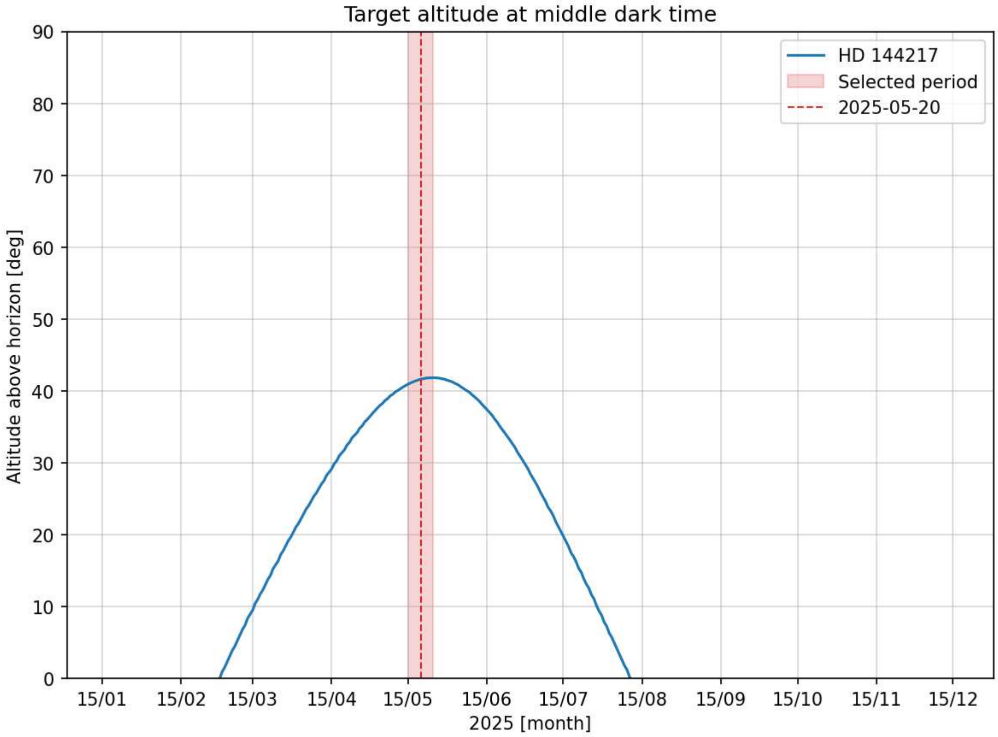

Fig. 4.11. *Best observation night for HD 144217. It was decided the period in which the target binary system is higher in the sky. The red rectangle shows the best period of the year for observing the system, while the red dotted line represents the selected night.*

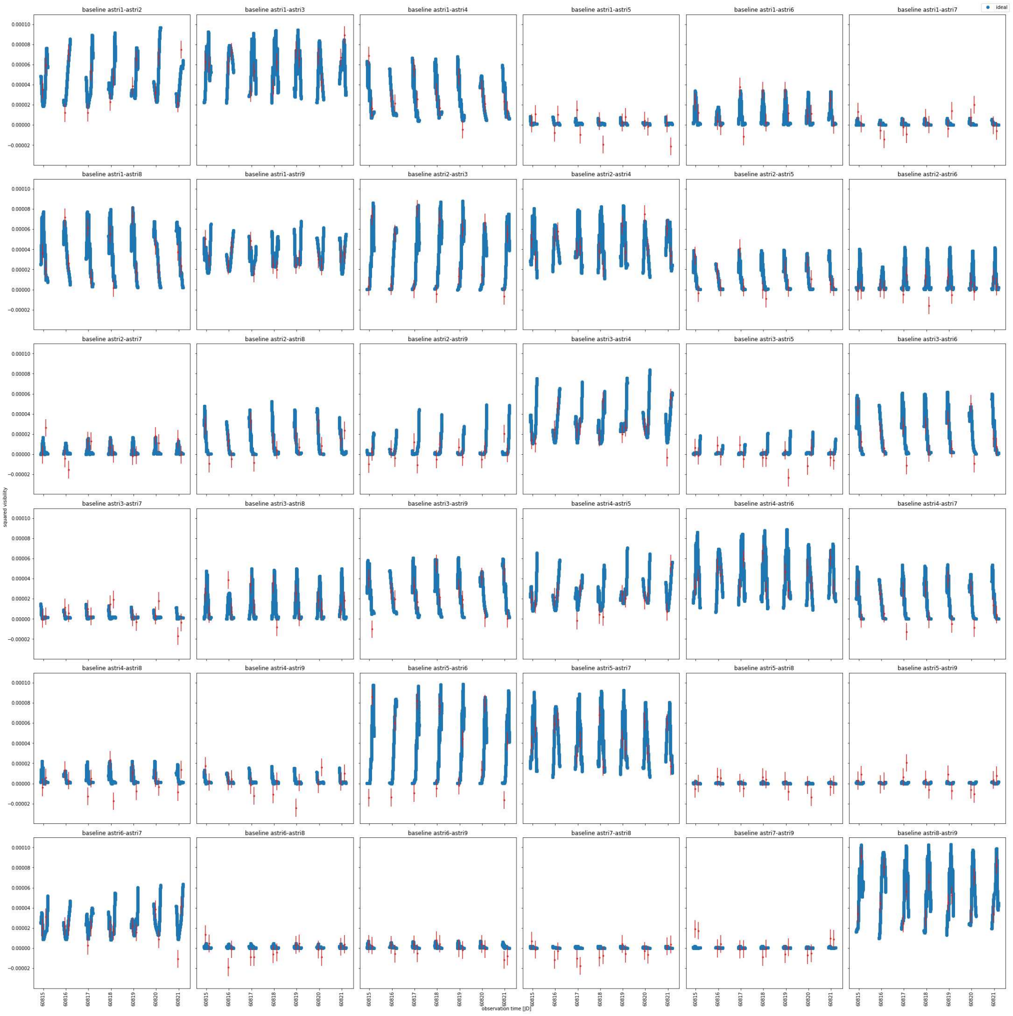

Fig. 4.12. *HD 144217 simulated observations. The blue lines represent the ideal correlation measured by the 36 baselines, while the red dots, and the respective error bars, represent the simulated observations.*

The fit has been performed only for four variables: the diameter of the two stars, the position angle, and the angular separation.
In the case of the simulation represented in Figure (4.12) the fitted diameters are d_1 = 0.422 ± 0.005 mas, and d_2 = 0.242 ± 0.037 mas, while the real diameters are d_1 = 0.422 ± 0.026 mas, and d_2 = 0.264 ± 0.019 mas, well within the errors.
In Figure (4.13) the true orbit, computed as explained in the "*simulateOrbit* function" section, and the fitted positions with their relative errors are shown.

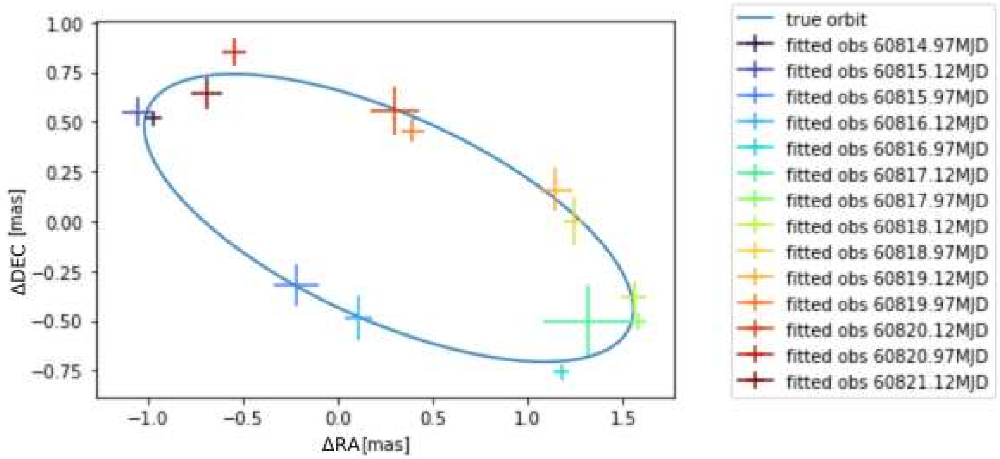

Fig. 4.13. *HD 144217 fitted positions on the true orbit of the system. The blue line represents the ideal orbit, computed using the binary system's real parameters, while the crossed dots represent the obtained points of the orbit using the fitted parameters.*

The fit precision can be increased by observing for a longer time interval (for example it would be possible to do one observation per night instead of two or three observations). In Figure (4.14) are shown the fitted positions obtained with this procedure.

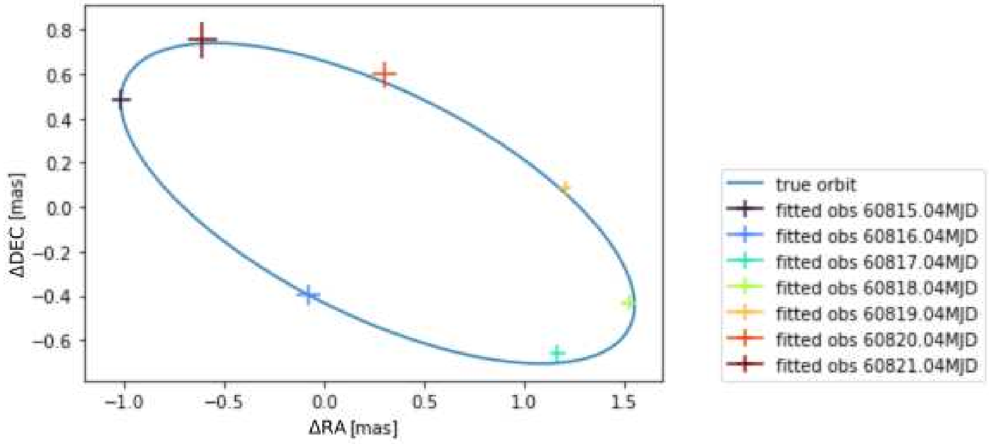

Fig. 4.14. *HD 144217 fitted positions on the true orbit of the system for 6 hours observations. The blue line represents the ideal orbit, computed using the binary system's real parameters, while the crossed dots represent the obtained points of the orbit using the fitted parameters.*

The results look very promising, being capable of characterizing the target system with the desired accuracy.

4.5 HD 37742 characterization

Being able to characterize HD 144217, it is expected to be able to characterize HD 37742. However, being the period much longer, the observations should be in a larger data frame. According to Figure (4.15), it was chosen as first night the 15/12/2025.

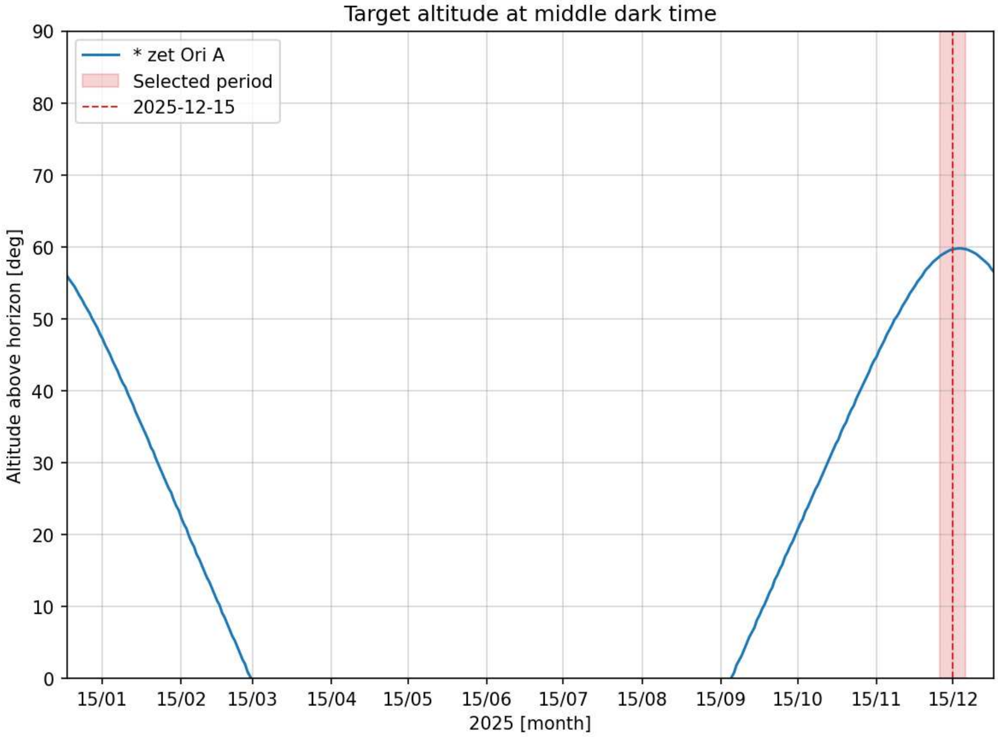

Fig. 4.15. *Best observation night for HD 37742. It was decided the period in which the target binary system is higher in the sky. The red rectangle shows the best period of the year for observing the system, while the red dotted line represents the selected night.*

Then, as explained in the previous section, an observation every three hours for the selected nights was simulated. The fitted positions are represented in Figure (4.16). These results are also very good.

In the case of the simulation represented in Figure (4.16) the fitted diameters are $d_1 = 0.54 \pm 0.01$ mas, and $d_2 = 0.45 \pm 0.03$ mas, while the real diameters are $d_1 = 0.54 \pm 0.01$ mas, and $d_2 = 0.45 \pm 0.12$ mas, well within the errors.

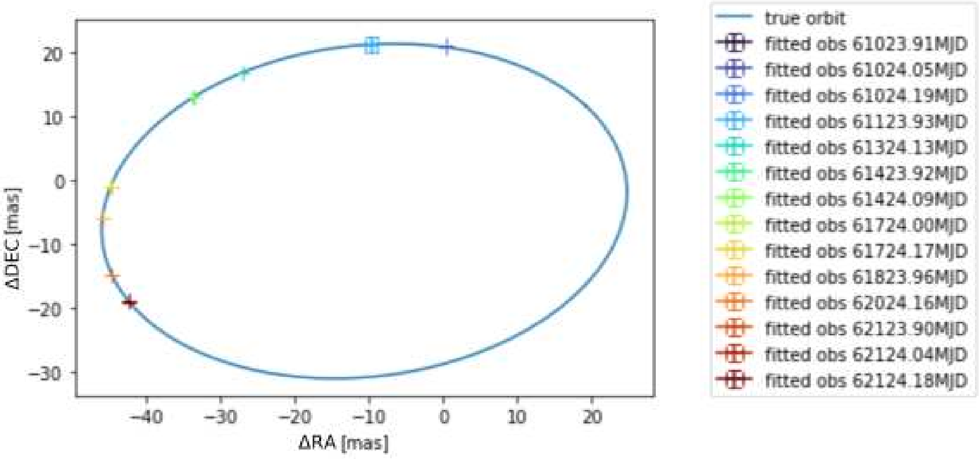

Fig. 4.16. *HD 37742 fitted positions on the true orbit of the system for 3 hours observations. The blue line represents the ideal orbit, computed using the binary system's real parameters, while the crossed dots represent the obtained points of the orbit using the fitted parameters.*

Chapter 5

Conclusions

In the first chapter of this thesis, the theory behind the physical phenomenon that led to the development of II was investigated and presented. Its understanding was fundamental for the development of the model presented in this thesis and for interpreting the results.

In the second chapter, a search in the scientific literature was conducted to see where in the astronomical field the II technique has already been implemented, and its various ways of use. This was really instructive, especially in seeing how research developed 70 years ago can now be revived and reused thanks to technological advances.

In the third chapter, the central work of this thesis is presented, which was the implementation and development of new theoretical models in a software dedicated to the simulation and analysis of scientific targets of SI3, the instrument that will perform II measurements for the ASTRI Mini-array. More precisely, the work carried out was to introduce a model for the interpretation of interferometric data in the case of observations of binary systems. The final outcome is a very versatile software that allows the simulation of a wide variety of cases, starting from the simple uniform disk model of a single star to a much more complex model of a binary system.

Finally, in the fourth chapter, the results obtained from the application of the software to several actual observable binary systems are presented. In particular, it is shown how the ASTRI Mini-array system is capable of characterizing binary systems up to a visual magnitude of ~3 with great accuracy, providing a method capable of characterizing such binary systems at wavelengths below 500 nm.

A possible further extension of the software would be to implement a fit that allows the orbital parameters of the binary system to be derived directly from the position angles and angular separations fitted from the observed squared visibility at different times, as this is not yet possible. However, deriving these parameters from interferometric measurements alone could be complicated. A possible solution could be to perform the measurements at different wavelengths or to complement the interferometric data with spectroscopic observations, as explained, for example, in [25]. Another possible future development of the software would be to include a module for 2D reconstruction of the images of the observed targets, starting directly from the correlation, without having to use any analytical model. This could even be used as a kind of 'digital twin' that could be linked to the observations in real time to check that everything is working correctly. In addition, the software developed can be easily extended to other arrays of telescopes with more baselines or bigger dishes, or to include multichannel interferometric measurements (measurements taken at different wavelengths during a single exposure). The latter implementation is particularly important as it would significantly increase the SNR and allow the study of fainter targets [42].

In conclusion, these results are very encouraging, both in terms of the results that will be possible to obtain as soon as the ASTRI Mini-array is operational and for future applications of the II.

Finally, it is clear from the analyses carried out in this thesis that the high angular resolution achievable with the ASTRI Mini-array will allow the study of various binary systems in great detail. The interferometric data, which can be complemented by spectroscopic and photometric data, will provide essential information to determine with great precision the fundamental parameters of the stars within these systems (such as masses and radii) and to study their evolution in great detail.

Appendix A

II analogical implementation

The setup used by Hanbury-Brown and Twiss (HBT) at the Narrabri observatory is shown in Figure 2.1. This consists of two collector mirrors, two interference filters, two photomultipliers, and a correlator. What was measured by HBT was therefore a correlation between currents, as depicted in Figure 2.2.
From this measure, the star diameter can be retrieved by relating the obtained correlation to the first order correlation function (i.e. the visibility) and then relating the visibility with the brightness distribution. This is done using the Van Cittert - Zernike theorem, described in equation (1.26).
Assume now that the signal currents $S_1(t)$ and $S_2(t)$ to be correlated are proportional to the time averages of $I_1(t)$ and $I_2(t)$ taken over short time T. Then it is possible to write:

$$S_1(t) = \frac{\alpha_1}{T}\int_{-\frac{1}{2}T}^{\frac{1}{2}T} I_1(t+t')dt' \,, \tag{A.1}$$

$$S_2(t) = \frac{\alpha_2}{T}\int_{-\frac{1}{2}T}^{\frac{1}{2}T} I_2(t+t')dt' \,, \tag{A.2}$$

where the constants α_1 and α_2 relate the photo current to the incident light intensity, representing the photocathodes photosensitivity. Then the unpolarized light correlation between the current fluctuations is:

$$\langle \Delta S_1(t)\Delta S_2(t)\rangle = \frac{1}{2}\frac{\langle S_1\rangle\langle S_2\rangle}{T^2}\int\int_{-\frac{1}{2}T}^{\frac{1}{2}T} |\gamma_{12}(t'-t'')|^2 dt'dt'' \,, \tag{A.3}$$

In the case the light spectrum is identical on the two detectors, the coherence function can be written as:

$$\gamma_{12}(\tau) = \gamma_{12}(0)\gamma_{11}(\tau) \,. \tag{A.4}$$

The integral of equation (A.3) can be expressed as a single integral, in the form:

$$\int\int_{-\frac{1}{2}T}^{\frac{1}{2}T} |\gamma_{12}(t'-t'')|^2 dt'dt'' = 2\int_0^T (T-t')\,|\gamma_{11}(t')|^2 dt' = T\xi(T) \,, \tag{A.5}$$

where $\xi(T)$ is equal to:

$$\xi(T) = \frac{2}{T}\int_0^T (T-t')\left|\gamma_{11}\left(t'\right)\right|^2 dt' \,. \tag{A.6}$$

as stated in [4].
Substituting it in equation (A.3), the correlation becomes:

$$\langle \Delta S_1(t)\Delta S_2(t)\rangle = \frac{1}{2}\langle S_1\rangle\langle S_2\rangle[\xi(T)/T]|\gamma_{12}(0)|^2 \,, \tag{A.7}$$

In the case of a simple rectangular filter and assuming $T \gg 1/\Delta\nu$, $\xi(T)/T$ can be written as:

$$\frac{\xi(T)}{T} = 2\frac{\Delta f}{\Delta\nu} \,, \tag{A.8}$$

where $\Delta\nu$ is the optical bandwidth, and $\Delta f \sim 1/T$ represents the bandwidth of a low pass filter with resolving time T.
Finally, it is now possible to write the equation (A.7) as:

$$\langle c(d)\rangle = \langle \Delta S_1(t)\Delta S_2(t)\rangle = e^2A^2\alpha^2n^2|\gamma_d(0)|^2\Delta\nu\Delta f \tag{A.9}$$

where $\langle c(d)\rangle$ is the correlation or time average of the multiplier output when the detectors are spaced by a distance d, A is the area of each detector, n is the intensity of the light in photons per unit optical bandwidth per unit area and unit time, and $|\gamma_d(0)|$ is the degree of coherence corresponding to $\tau = 0$ and a baseline d. From the previous equation, it is possible to see that the correlation observed at any given baseline d is proportional to $|\gamma_d(0)|^2$ the square of the modulus of the complex degree of coherence. This is the equation with which Hanbury-Brown and Twiss measured more than thirty stars diameter at Narrabri.

Appendix B

Momentum analysis

From the properties of the Poisson distribution, it is possible to identify the moment generating function $M_n(x)$ of the distribution of n as:

$$M_n(x) = \langle exp[\alpha E(e^x - 1)] \rangle \;, \tag{B.1}$$

where $\langle\rangle$ denotes the ensemble average over the random variable E. By representing the moment generating function of the distribution of E as $M_E(x)$, equation (B.1) can be written as:

$$M_n(x) = M_E(\alpha e^x - \alpha)\,, \tag{B.2}$$

from which it is possible to write:

$$K_n(x) = K_E(\alpha e^x - \alpha)\,, \tag{B.3}$$

or:

$$\sum_{i=1}^{\infty} \frac{x^i}{i!} k_{ni} = \sum_{i=1}^{\infty} \frac{\alpha^i \left(e^x - 1\right)}{i!} k_{Ei}\,, \tag{B.4}$$

where $K_n(x)$ and $K_E(x)$ are the corresponding cumulant generating functions, and k_{ni} and k_{Ei} are the cumulants of the distributions of n and E. By means of the cumulants k_{Ei} found in [39], equation (B.4) allows to write the cumulants k_{ni} of the distribution of n. It can be shown [40] that:

$$k_{n1} = \alpha k_{E1}\,, \tag{B.5}$$

$$k_{n2} = \alpha k_{E1} + \alpha^2 k_{E2}, \ldots, \tag{B.6}$$

where:

$$k_{Ei} = \begin{cases} \langle E \rangle = \langle I \rangle T & i = 1 \\ (i-1)! \langle I \rangle^i \int \int_{-\frac{1}{2}T}^{\frac{1}{2}T} \ldots \int \gamma_{11}(t_1 - t_2)\gamma_{11}(t_2 - t_3) \ldots \gamma_{11}(t_i - t_1) dt_1 dt_2 \ldots dt_i & i \neq 1 \end{cases} . \tag{B.7}$$

These cumulants define the counting distribution of n and are equivalent to an explicit expression for $p(n, T)$. Two limiting cases are of particular interest. If the mean light intensity $\langle I \rangle$ is extremely low, all the terms k_{ni} tend to become small compared with the first term $\alpha K_{E1} = \alpha \langle I \rangle T = \langle n \rangle$. It follows that the cumulants of the counting distribution $p(n, T)$ all tend to $\langle n \rangle$, which means that the distribution becomes Poissonian. Thus, at very low beam intensities, the photons behave like classical particles in their statistical properties. On the other hand, at high intensities, when $\alpha\langle I \rangle$ becomes very great, the last term becomes dominant in each k_{ni}, so the distribution of n tends to become identical with the distribution of αE.

Now, the variance $\left\langle \Delta n^2 \right\rangle$ of the counting distribution $p(n, T)$, is identical with the second cumulant k_{n2}, thus:

$$\left\langle \Delta n^2 \right\rangle = \alpha \langle I \rangle + \alpha^2 \langle I^2 \rangle \int \int_{-\frac{1}{2}T}^{\frac{1}{2}T} |\gamma_{11}(t_1 - t_2)|^2 \, dt_1 dt_2 = \langle n \rangle [1 + \langle n \rangle \xi(T)/T]\,, \tag{B.8}$$

where:

$$\langle n \rangle = \alpha \langle I \rangle T \,, \tag{B.9}$$

and

$$\frac{\xi(T)}{T} = \frac{1}{T^2} \int \int_{-\frac{1}{2}T}^{\frac{1}{2}T} |\gamma_{11}(t_1 - t_2)|^2 dt_1 dt_2 \,. \tag{B.10}$$

Appendix C

The *emcee* package

This python package is based on the affine invariant ensemble sampler for Markov Chain Monte Carlo (MCMC) proposed by [41]. This algorithm is informally called the "stretch move", and it significantly outperforms the standard Metropolis-Hastings (M-H) methods.

This method simultaneously evolves an ensemble of K walkers, $S = \{X_k\}$, where the proposal distribution for one walker k is based on the current positions of the $K - 1$ walkers in the complementary ensemble $S_{[k]} = \{X_j, \forall j \neq k\}$. To update the position of a walker at position X_k, a walker X_j is drawn randomly from the remaining walkers $S_{[k]}$ and the new position proposed is:

$$X_k(t) \to Y = X_j + Z[X_k(t) - X_j]\,, \tag{C.1}$$

where Z is a random variable drawn from a distribution $g(Z = z)$. In the case g satisfies:

$$g\left(z^{-1}\right) = zg(z)\,, \tag{C.2}$$

equation (C.1) is symmetric. In this case, the chain satisfies detailed balance if the proposal is accepted with probability

$$q = min\left(1, Z^{N-1}\frac{p(Y)}{p(X_k(t))}\right)\,, \tag{C.3}$$

where N is the dimension of the parameter space. This procedure is then repeated for each walker in the ensemble in series.

The stretch move algorithm can be parallelized by splitting the full ensemble into two subsets $S^{(0)} = \{X_k, \forall k = 1, ..., K/2\}$ and $S^{(1)} = \{X_k, \forall k = K/2 + 1, ..., K\}$ and simultaneously updating all the walkers in $S^{(0)}$ based only on the positions of the walkers in the other set $S^{(1)}$. Then, using the new positions $S^{(0)}$, it is possible to update $S^{(1)}$. The pseudocode for this procedure is shown in Algorithm 1.

Algorithm 1 Parallelized stretch move algorithm

```
for $i \in \{0, 1\}$ do
    for $k = 1, ..., K/2$ do
        // This loop can now be done in parallel for all $k$
        // Draw a walker $X_j$ at random from the complementary ensemble $S^{(\sim i)}(t)$
        $X_k \leftarrow S^{(i)}_k$
        $z \leftarrow Z \sim g(z)$
        $Y \leftarrow X_j + z[X_k(t) - X_j]$
        $q \leftarrow z^{n-1} p(Y)/p(X_k(t))$
        $r \leftarrow R \sim [0, 1]$
        if $r \leq q$ then
            $X_k(t + 1/2) \leftarrow Y$
        else
            $X_k(t + 1/2) \leftarrow X_k(t)$
        end if
    end for
    $t \leftarrow t + 1/2$
end for
```

Bibliography

[1] Hanbury B. R., et al., A new type of interferometer for use in radio-astronomy, Phil. Mag., 45, 663, (1954).

[2] Mandel L., Fluctuations of light beam, Progress in Optics, Volume 2, Pages 181-248, (1965)

[3] Purcell E. M., The Question of Correlation between Photons in Coherent Light Rays, Nature, Volume 178, Pages 1449–1450,(1956).

[4] Rice S. O., Mathematical Analysis of Random Noise, The Bell System Technical Journal, Volume 23, Issue 3, (1945).

[5] Glauber R., Photon correlations, Phys. Rev. Lett. 10, 3, (1962).

[6] Zernike F., The concept of degree of coherence and its application to optical problems, Physica, Volume 5, Issue 8, Pages 785-795, (1938).

[7] Hanbury B. R., Intensity Interferometer, Taylor & Francis, Halsted Press, (1974).

[8] Hanbury B. R., The Angular Diameters of 32 Stars, Monthly Notices of the Royal Astronomical Society, Volume 167, Pages 121-136, (1974).

[9] https://web.oapd.inaf.it/zampieri/aqueye-iqueye/.

[10] Barbieri C., Aqueye and Iqueye, Very-High-Time-Resolution Photon-Counting Photometers, Proceedings of the International Astronomical Union, 7(S285), Pages 280-282, (2012).

[11] Zampieri L. et al., (Very) Fast astronomical photometry for meter-class telescopes, Contributions of the Astronomical Observatory Skalnaté Pleso, Volume 49, Number 2, Pages 85-96, (2019).

[12] Zampieri L., et al., Stellar intensity interferometry of Vega in photon counting mode, MNRAS, Volume 506, Issue 2, Pages 1585–1594, (2021).

[13] Zampieri L., et al., A stellar intensity interferometry instrument for the ASTRI Mini-Array telescopes, SPIE, Conference: Optical and Infrared Interferometry and Imaging VIII, (2022).

[14] Bonanno G., et al., Focal plane detector and front-end electronics of the stellar intensity interferometry instrument for the ASTRI Mini-Array telescopes, SPIE, Proceedings Volume 12183, Optical and Infrared Interferometry and Imaging VIII, (2022).

[15] Haguenauer P. et al., The very large telescope Interferometer: 2010 edition, Proceedings of the SPIE, Volume 7734, (2010).

[16] Scuderi S., The ASTRI Mini-Array of Cherenkov telescopes at the Observatorio del Teide, Journal of High Energy Astrophysics, Volume 35, Pages 52-68, (2022).

[17] Ahnen M. L. et al., Performance of the MAGIC telescopes under moonlight, Astroparticle Physics, Volume 94, Pages 29-41, (2017).

[18] Kasseli et al., An Empirical Template Library of Stellar Spectra for a Wide Range of Spectral Classes, Luminosity Classes, and Metallicities Using SDSS BOSS Spectra, The Astrophysical Journal Supplement Series, Volume 230, Number 2, (2017).

[19] Berger J.P., An introduction to visibility model, New Astronomy Reviews, Volume 51, Issues 8–9, Pages 576-582, (2007).

[20] Ségransan D., Observability and UV coverage, New Astronomy Reviews, Volume 51, Issues 8–9, Pages 597-603, (2007).

[21] Naletto et al., A 3.9 km baseline intensity interferometry photon counting experiment, SPIE, Conference: SPIE Optical Engineering + Applications, (2016).

[22] Foreman-Mackey D. et al., emcee: The MCMC Hammer, Publications of the Astronomical Society of the Pacific, Volume 125, Number 925, (2013).

[23] Hogg D. W. et al., Data analysis recipes: Fitting a model to data, arXiv:1008.4686, (2010).

[24] Diaz-Castro F. J., Adaptation of streetlighting on La Palma, New Astronomy Reviews Volume 42, Issues 6–8, Pages 509-513, (1998).

[25] Bonneau D. et al, Observation of double star by long baseline interferometry, EAS Publications Series, Volume 69-70, (2014).

[26] Fiori M. et al., Investigating the accuracy achievable in reconstructing the angular sizes of stars through stellar intensity interferometry observations, Astronomy & Astrophysics, Volume 666, ID:A48, (2022).

[27] Carroll B. et al., An Introduction to Modern Astrophysics, Pearson New International Edition, (2013).

[28] Hummel C. A. et al., ζ Orionis A is a double star, The Astrophysical Journal, Volume 540, Pages L91-L93, (2000).

[29] Hummel C. A. et al., Dynamical mass of the O-type supergiant in Zeta Orionis A, A&A 554, A52, (2018).

[30] Martinod M. A. et al., Fibered visible interferometry and adaptive optics: FRIEND at CHARA, A&A 618, A153, (2018).

[31] Holmgren D. et al., Search for forced oscillations in binaries II. β Scorpii A. New physical parameters and a search for line profile variability, Astron. Astrophys. 322, Pages 565–575, (1997).

[32] Elliot J. L. et al., The occultation of '*beta* Scorpii by Jupyter. VII. The angular diameters of '*beta* Scorpii A_1 and A_2, The Astrophysical Journal, Volume 207, Pages 994-1001, (1976).

[33] Turner N. H. et al., Adaptive optics photometry and astrometry of binary stars. III. A faint-companion search of O-star systems, The Astronomical Journal, Volume 136, Number 2, (2008).

[34] Kharchenko N. V., All-sky compiled catalogue of 2.5 million stars, Kinematika i Fizika Nebesnykh Tel, Volume 17, Number 5, Pages 409-423, (2009).

[35] Abt H. A. et al., Rotational velocities of B stars, The Astrophysical Journal, Volume 573, Pages 359–365, (2002).

[36] Gordon K. D. et al., Angular Sizes and Effective Temperatures of O-type Stars from Optical Interferometry with the CHARA Array, The Astrophysical Journal, Volume 869, Number 1, (2018).

[37] Gies D. R. et al., The binary frequency and origin of the OB runaway stars, The Astrophysical Journal Supplement Series, 61:419-454, (1986).

[38] Evans D. S., Occultation Astrometry of the Beta Scorpii System, The Astronomical Journal, Volume 83, Number 4, (1978).

[39] Slepian D., Fluctuations of Random Noise Power, Bell System Technical Journal, Volume 37, Issue 1, Pages 163-184, (1957).

[40] Mandel L., Fluctuations of Photon Beams: The Distribution of the Photo-Electrons, Proceedings of the Physical Society, Volume 74, Number 3, (1959).

[41] Goodman J. et al, Ensemble Samplers with Affine Invariance, Communications in Applied Mathematics and Computational Science, Volume 5, Number 1, (2010).

[42] Trippe et al., Optical Multi-Channel Intensity Interferometry - or: how to resolve O-Stars in the Magellanic Clouds, Journal of The Korean Astronomical Society, Volume 47, Issue 6, Pages 235-253, (2014).